



Direct molecular dynamics simulation of piezoelectric and piezothermal couplings in crystals

Wassim Kassem

► To cite this version:

Wassim Kassem. Direct molecular dynamics simulation of piezoelectric and piezothermal couplings in crystals. Other. Ecole Centrale Paris, 2015. English. NNT : 2015ECAP0043 . tel-01247219

HAL Id: tel-01247219

<https://theses.hal.science/tel-01247219>

Submitted on 4 Jan 2016

HAL is a multi-disciplinary open access archive for the deposit and dissemination of scientific research documents, whether they are published or not. The documents may come from teaching and research institutions in France or abroad, or from public or private research centers.

L'archive ouverte pluridisciplinaire **HAL**, est destinée au dépôt et à la diffusion de documents scientifiques de niveau recherche, publiés ou non, émanant des établissements d'enseignement et de recherche français ou étrangers, des laboratoires publics ou privés.

THÈSE

présentée par

Wassim Kassem

pour l'obtention du

GRADE de DOCTEUR

Formation doctorale : Physique et Sciences pour l'Ingénieur

Laboratoire d'accueil : Laboratoire d'Énergétique Moléculaire
et Macroscopique, Combustion (EM2C)
du CNRS et de l'ECP

Direct Molecular Dynamics Simulation of Piezoelectric and Piezothermal Couplings in Crystals

Soutenue le 15 septembre 2015

Jury : M Volz S. Directeur de thèse

MERABIA S. Rapporteur

KAZAN M. Rapporteur

PERRIN B.

DKHIL B.

CHALOPIN Y.

Remerciements

The thesis presented here could not have been without the support of several people. First and foremost, my the greatest thanks goes to my adviser Dr. Sebastian Volz. Working with him was an honor. I thank him for his incisive and valuable advice during the time I spent at EM2C, and more so during the last few months of the thesis when his support was invaluable to me finishing. I hope I can repay his confidence and patience with success someday. I would also like to thank Prof. Emmanuel Ollier who supported us from CEA. I always enjoyed his insights and advice during the few but precious meetings we had over the phone or face to face.

To Dr. Yann Chalopin I would also like to single out a special thank you. From day one when he helped me calculate the phonon density of states for the first time to the last day of the thesis defense. It was a pleasure to watch him work. I hope to match his energy and intelligence one day.

To Dr. Michel Kazan, thank you for always supporting me. He was the reason for my sanity during difficult times. He is a remarkable scientist and person. His generosity when it comes to his time and effort with his students is unmatched. He is responsible for the careers of many Lebanese scientists. I hope I will be able to repay him as well for his help, and to be able to work with him in the near future.

To the committee members who agreed to participate, my deepest thanks; especially the reporters whose quick response and patience made this possible. I apologize for the delays and thank them for all their efforts.

To my friends in the group: Benoit, Jordane, Haxoue, Yunhui, Kimmo, Yuxiang, and Shiyun especially for his support during my compiling of the thesis. To Sergei for his support during the day of the defense. To Laurant and Jose. Thank you all.

To my friends in the lab, Macole S., a huge thanks and debt of gratitude are due. Thanks to you for always being there to support and encourage me. To Gizem and Pedro I say best of luck! To David C. who I met not soon enough. The secretarial staff as well, Nathalie R. was the lab angel and go-to person for all the PhDs.

Finally, to my dear family in Lebanon. To my dad who helped me in times of need. I hope I have made you proud. To my sisters, Razan and Shereen, my love and thanks for their support.

Abstract

The thesis is focused on investigating the effect of strain on the thermal conductivity of piezoelectric materials. Piezoelectric materials are crystals which display a mechanical deformation upon application of an electric field. Examples of such material are ZnO, AlN, and SiO₂. Using Molecular Dynamics simulations, we calculate the thermal conductivity of unstrained and strained ZnO and AlN crystals. We also calculate the thermal resistance of SiO/graphene interfaces under strain.

We calculate the piezoelectric and elastic properties of ZnO. These will serve as confirmation of the correctness of the inter-atomic potential used, and will serve to show the magnitude of strain that is possible to apply. Using non-equilibrium molecular dynamics, we determine the elastic coefficient of ZnO c_{33} , and we see that it agrees with experimental values. We also determine that the elastic limit of a perfect ZnO crystal is 6 GPa which corresponds to a 6% strain. We also determine the piezoelectric coefficient of ZnO using NEMD, and we find that the piezoelectric coefficient d_{33} also agrees with literature values.

Second, we look at the effect of strain on the intrinsic thermal conductivity of ZnO and AlN. We use reverse non-equilibrium molecular dynamics to calculate the conductivity because the computational costs are significantly lower than those for the equilibrium method; especially for ZnO whose inter-atomic potential contains Coulomb interaction.

We also study the size-effect on the thermal conductivity of ZnO and AlN. We show that the Schelling formula can indeed be implemented to both crystals for different values of strain. The infinite length thermal conductivity for ZnO is extracted from the formula, and it is found to be 410 W/mK. We then calculate the thermal conductivity of strained ZnO crystals. We show that after correcting for the size effect the thermal conductivity follows a power-law dependence to uniaxial strain. Also, we demonstrate that the thermal conductivity of ZnO can be affected by a static external field due to the induced strain.

The infinite length thermal conductivity of AlN is found to be 3000 W/mK. We show that for the case of AlN the effect of strain does not affect the thermal conductivity due to the different inter-atomic bonding. Hence, AlN might not be a useful material for piezothermal application.

Third, we explore the effect of piezoelectric strain on the thermal conductance of SiO₂/graphene and ZnO/graphene superlattices. Using EMD we calculate the thermal conductivity of a superlattice composed of silica and graphene monolayers. The thermal conductance of the superlattice was evaluated under different values of external electric field. We find that applying a positive electric field parallel to the

Z-direction leads to reduction of the thermal conductance by a factor of 2 for an electric field of 20 MV/m. On the other hand, no change in the thermal conductance is noted for ZnO/graphene superlattice. The effect is due to the non-uniform strain induced at the superlattice junctions. The effect is recreated in Si/Ge superlattice by mechanically applying a non-uniform strain at the interface. This approach might be responsible for the scattering of phonons.

Résumé

La thèse est axée sur l'examen de l'effet de la contrainte sur la conductivité thermique des matériaux piézoélectriques. Les matériaux piézoélectriques sont des cristaux qui présentent une déformation mécanique lors de l'application d'un champ électrique. Des exemples de tels systèmes sont ZnO, AlN, et SiO₂. En utilisant des simulations de dynamique moléculaire, nous avons calculé la conductivité thermique de cristaux de ZnO et AlN sous contrainte. Nous avons aussi calculé la résistance thermique des interfaces SiO/C et ZnO/C soumis à un champ électrique.

Nous commençons par le calcul des propriétés piézoélectriques et élastiques de ZnO. Celles-ci serviront à valider les potentiels interatomiques utilisés, et à montrer l'ampleur de la contrainte qu'il est possible d'appliquer. En utilisant la dynamique moléculaire d'équilibre, nous avons estimé le coefficient élastique c_{33} de ZnO, qui se trouve être en accord avec les valeurs expérimentales. Il a aussi été déterminé que la limite élastique d'un cristal de ZnO est de 6 GPa, ce qui correspond à une déformation de 6

Deuxièmement, nous avons examiné l'effet de la pression sur la conductivité thermique intrinsèque de ZnO et d'AlN. La dynamique moléculaire de non-équilibre inverse a été mise en œuvre pour calculer la conductivité parce que les coûts de calcul sont nettement inférieurs à ceux de la méthode d'équilibre, d'autant plus pour ZnO dont le potentiel inter-atomique contient les interactions Coulombiennes. L'effet de taille sur la conductivité thermique de ZnO et AlN a ensuite été étudié. Nous avons montré que la formule de Schelling peut en effet être mise en œuvre pour les deux cristaux pour différentes valeurs de la contrainte. La conductivité thermique pour un cristal de ZnO de taille infinie est extraite de la formule de Schelling, et elle se révèle être de 410 W/mK. La conductivité thermique de cristaux de ZnO sous contrainte a ensuite été analysée. Nous avons montré que, après correction de l'effet de taille, la conductivité thermique suit une dépendance en loi de puissance à la contrainte uniaxiale. De plus, la conductivité thermique de ZnO est affectée par un champ statique externe en raison de la contrainte induite. La conductivité thermique d'AlN est estimée à 3000 W/mK, l'effet de la contrainte ne modifie pas cette valeur du fait du potentiel inter-atomique utilisé. Par conséquent, AlN n'est pas un matériau pertinent pour faire office de switch thermique.

Troisièmement, nous avons exploré l'effet d'un déplacement piézoélectrique sur la conductance thermique d'interface de SiO₂/graphène et ZnO/graphène. Utilisant la dynamique moléculaire d'équilibre, la conductivité thermique d'un super-réseau dont la période est composée de silice et de graphène polyfeuillet. Le super-réseau a été évalué pour différentes valeurs du champ électrique externe. Nous avons constaté que l'application d'un champ électrique de 20 MV/m positif parallèle à la direction hors-plan du super-réseau conduit à la réduction de la conductivité thermique d'un

facteur deux. D'autre part, aucun changement dans la conductance thermique n'est noté pour le super-réseau ZnO/graphène. Cette différence est due aux différences de déformations induites au niveau des interfaces dans le super-réseau. L'effet est recréé dans un super-réseau Si/Ge en appliquant une déformation pour former les interfaces. Cette approche crée une déformation non uniforme qui est susceptible de diffuser les phonons.

Contents

Abstract	v
Résumé	vii
1 Introduction	1
1.1 Thermal management in the semiconductor industry	1
1.2 Static and transient thermal management	4
1.3 Physical background behind solid-state switches	7
1.4 Piezoelectric crystals	12
1.5 Organization of the thesis	15
2 Molecular Dynamics	17
2.1 Introduction	17
2.2 Physical principles of Molecular Dynamics	18
2.3 Thermal and mechanical macroscopic quantities	26
2.4 Physical limitations and conclusions	30
3 Origin of thermal conductivity changes in bulk material. Effect of uniaxial strain	31
3.1 Description of simulation procedure	31
3.2 Thermal conductivity of bulk ZnO crsytals	35
3.3 Thermal conductivity of bulk AlN crystals	43
3.4 Conclusions	46
4 Thermal conductance - Kapitza resistance. Effect of local strain on thermal conductance of superlattices	47
4.1 Literature review	47
4.2 Effect of non-uniform strain on the thermal conductance of SiGe superlattices	51
4.3 Molecular Dynamics simulation of the thermal conductance of SiO ₂ /FLG superlattices	54
4.4 Molecular dynamics simulations of ZnO/FLG superlattices	58
4.5 Conclusions	60
5 Conclusions and future work	63
5.1 Conclusions	63
5.2 Future works, perspective, and issues	64
References	73

List of Tables

2.1	List of common MD potentials used in this work	20
2.2	Coefficients for inter-atomic potential representing ZnO	22
2.3	Comparison of the lattice parameters and elastic constants of ZnO obtained using different methods.	24
2.4	Parameters for the PCRRM potential for ZnO. Taken from Wang et al. (2014).	24
2.5	Formulas for thermal and mechanical quantities calculated during a MD simulation. k refers to the Boltzmann constant and N to the number of kinetic degrees of freedom.	27
3.1	Debye temperature of ZnO at room temperature from different sources available in literature.	36
4.1	Thermal conductance results for the various simulation types of SiGe superlattices. The errors are the standard deviations of the averages during the data collection period. P_z is the average pressure at the end of the simulation.	54
4.2	Thermal boundary resistance of ZnO/C as a function of electric field strength.	60

List of Figures

1.1	Plot showing the increase in transistor density and power loss in Intel processors from Holzer (2007)	2
1.2	schematic diagram of a microprocessor showing its main components, and the abundance of interfaces where heat is generated from Schelling, Shi, and Goodson (2005)	3
1.3	Phonon spectrum and its applications. Figure from Maldovan (2013)	3
1.4	A MEMS thermal switch schematic and real-life counterpart. Adapted from Cho et al. (2008)	5
1.5	(a) Figure showing the single layer SiN three-strip actuator, (b) Scanning electron micrograph of a specimen, (c) Strain is measured post-experiment fracture of the specimen. Adapted from Alam et al. (2015)	6
1.6	A two-atomic linear chain with lattice constant $2a$ and masses m and M ($m < M$) at the equilibrium position from Srivastava (1990)	7
1.7	Dispersion relation for linear diatomic chain.	9
1.8	Thermal conductivity as a function of temperature for some typical materials.	13
1.9	Values of piezoelectric constants for some typical materials from Newnham (2005)	14
2.1	Representation of the basic element of a MD cell where atoms are interacting through potential forces. Periodic boundary conditions are used to induce a translational symmetry and mimic an infinite size system.	19
2.2	Comparison of dispersion relations and vibrational density of states for ZnO calculated using MD and lattice statistics at 0K. The white points/curve represents the ab initio data, and the dark lines/curve represent our calculating using MD for the DOS and lattice dynamics for the dispersion curves.	23
2.3	Parameters for the Vashishta potential for AlN taken from Vashishta et al. (2011)	25
2.4	Comparison of the vibrational density of states of AlN calculated using MD and the Vashishta potential to the one found in Vashishta et al. (2011)	26
2.5	An example of heat flux autocorrelation function with the fitting of different methods. The insert represents the integral of the thermal conductivities over time. Figure from McGaughey and Kaviany (2004)	28
2.6	The inverse of the thermal conductivities measured with NEMD simulations for Si and diamond at specified temperatures versus $1/L$ and the corresponding fitting with Eq. 2.15. κ_∞ is get at $1/L = 0$. Figure from Schelling et al (2002) , Phys. Rev. B 65: 144306	29

3.1	Perspective images of $4 \times 8 \times 20$ uc ZnO crystal after initialization. The silver and red atoms represent zinc and oxygen atoms respectively. . .	33
3.2	A representative temperature profile at 300K, -2% strain after 500ps of applying the Muller-Plathe algorithm.	34
3.3	Schematic representing the Muller-Plathe algorithm	34
3.4	Dependence of thermal conductivity on the length of the MD simulation cell. The thermal conductivity of the infinite system is deduced from the value extrapolated when the reverse of the length goes to zero. . .	37
3.5	Pressure versus strain for $7 \times 4 \times 20$ ZnO crystal at 300K. The strain and pressure are averaged over the data collection period. The straight line represents the linear fit of the data with the intercept fixed at zero. . .	38
3.6	Effect of strain on the thermal conductivity of ZnO bulk crystals . . .	39
3.7	Thermal conductivity corrected for size effect as a function of strain at 300K. The red line represents the fitting of the data to a power law function.	40
3.8	Phonon mode properties as a function of strain along the [0001] direction	41
3.9	Strain versus electric field strength along the c-direction. The straight line represents the linear fit of the data where α is the slope and β is the y-intercept.	42
3.10	A representative graph of the temperature gradient of a $14 \times 8 \times 20$ AlN crystal at 300K during the data collection period. This is after 500 ps of applying the heat flux.	43
3.11	Effect of system length on the calculated thermal conductivity of AlN at 300K for 0 and -3% strain. The straight lines are the linear fit to the data with α as the slope and β representing the y-intercept.	44
3.12	Effect of strain on the calculated thermal conductivity of AlN at room temperature.	45
4.1	A schematic showing the dislocation due to mismatched lattices. The black dots and red circles represent the atom positions on the two lattices. S_b , S_a are the contact planes, and p is the distance between dislocations. It also represents the dissimilarity between the two lattices. Smaller p indicates more dissimilarity. From Meng et al. (2013)	49
4.2	Perspective and in-plane view of SiGe superlattice $10 \times 10 \times 20$ before start of simulation. Ge atoms are in yellow and Si atoms are in pink. .	52
4.3	Temperature profiles for the different simulation types of the SiGe superlattice. The profiles shown are collected at the end of the simulation.	53
4.4	A schematic showing the rescaling of the simulation box for the case of tensile strain. The figure is to scale in the Z-direction; however, the rescaling is exaggerated for clarity. The operation is performed after the equilibration period, and the superlattice is allowed to relax under NVT conditions. The arrows represent the restoring forces arising from the remapping of the atoms.	53
4.5	A snapshot of silica/graphene superlattice used for all simulations with 3 monolayers of graphene (green atoms) and 7 unit cells of silica or α -quartz. The electric field is applied in the cross-plane direction. . . .	55
4.6	Schematic representation of the SiOC superlattice with the application of an electric field leading to local compressive strain at the interfaces. The arrows represent the electrostatic forces at the end surfaces. Figure not to scale.	56

4.7	The thermal boundary resistance as a function of simulation time for several electric field strengths in MV/m.	57
4.8	Snapshots of ZnO/C superlattice at different stages of the simulation with and without an external electric field. Carbon atoms are in green, and are placed on the Zn face. Note the reconstruction of the ZnO lattice at the free ends.	58
4.9	Temperature profiles of ZnO/C superlattices at the end of the simulations for different electric field strengths. The first point corresponds to the temperature of the double monolayers of graphene (cold slab). .	59

Chapter 1

Introduction

1.1 Thermal management in the semiconductor industry

1.1.1 Motivation

Microprocessors Significant enhancements in device fabrication and integration in the electronics industry have led to a rapid increase in the total power consumption in electronic circuits. Transistors which form the basic building blocks for microprocessors for example have been reduced to a few nm within four decades. This has allowed manufacturers to pack more of them onto a single die. One of the beneficial aspects of this higher density packing is a reduction in signal propagation delays, permits higher clock-frequencies, and as such better performance. If we take microprocessors for example; today's processors are faster and cheaper than older ones by several orders of magnitude owing to the exponential growth in transistor density. The scaling has surpassed the growth predicted by Gordon Moore's empirical law stated in 1965 ([Moore \(2006\)](#)) which stated that processor transistor density would double every year.

However, in his paper, Moore also indicated that it would also be possible to cool integrated circuits efficiently due to the relatively large surface area of integrated circuits, and the limited number of components that need to be driven. Dennard scaling justifies this by indicating that to keep the electric field constant in a reduced transistor, the voltage would have to be reduced as well thus reducing the power consumption ([Dennard et al. \(1974\)](#)). In fact, today this scaling has broken down, and we know that this is no longer true. In fact, voltage leakage which leads to heating is the most acute problem facing the advancement of current integrated circuit technology ([McMenamin \(2013\)](#)). 50% of the energy consumed by a microprocessor is dissipated as heat due to its electrical resistance and/or current leakage. This leads to negative effects on the lifetime and performance of these microprocessors. In fact, the surface density power of microprocessors was approaching that of nuclear plants ([Taylor \(2009\)](#)) as seen in Figure 1.1.

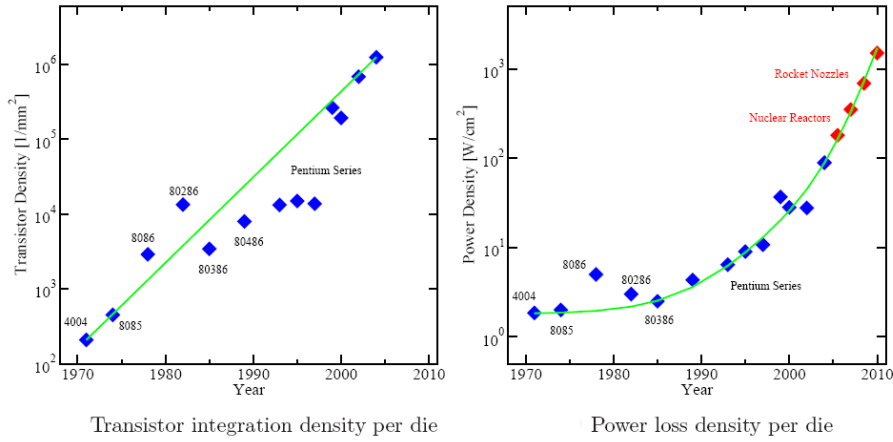


Figure 1.1: Plot showing the increase in transistor density and power loss in Intel processors from [Holzer \(2007\)](#)

LEDs Another electronic device which is also prone to heating issues is LEDs. Lighting based LEDs has become an important issue of the current decade due to LEDs becoming a competitor to conventional lighting sources such as incandescent and fluorescence based lighting. Today, the efficiencies of LEDs exceed 50% [Müllen and Scherf \(2006\)](#), and all colors of the visible spectrum are available using different combinations of semiconductors. The lifetimes of LEDs (10^5 hrs) also compare favourably with incandescent sources (500h) and fluorescent sources (5000 h). To achieve high quantum efficiency in a LED, free carriers need to be spatially confined. The light extraction efficiency has also proven to be a key factor in increasing the efficiency of high power LEDs. The maximum thermal power that may be dissipated in a LED is determined by the maximum operating temperature and the thermal resistivity of the LED package. High-power LEDs thus require lower thermal resistivity packaging. However, active cooling is not used in these LEDs as it would lead to lower power efficiency. Rather passive-based cooling is preferred where heat is transported to the printed circuit board using metal heat sink slugs ([Müllen and Scherf \(2006\)](#)). Lighting based LED therefore can suffer from the negative effects of overheating, and it is necessary to reduce the thermal resistivity of the packaging ([Weng \(2009\)](#)). Most of the electrical energy consumed by a LED is transformed to heat; almost 70%, and if the temperature of a LED rises above the recommended threshold then its reliability and lifetime is considerably reduced ([Yuan et al. \(2006\)](#)).

Hence, heat management is an issue for LEDs as well; however, this issue of overheating in microelectronics can perhaps be turned into a positive outcome. In fact, if we note the omnipresence of electronics in daily life, it becomes apparent that improving the efficiency and giving more thought into controlling the heat losses in these circuits is a crucial need. The reduction of heat damage to electronic components would lead to increased lifetime, less waste energy, and perhaps even the transformation of heat waste into electrical energy.

Current thermal management or thermal protection methods are macroscopic scale and package level. Heat sinks, fans, and other devices attempt to control the tem-

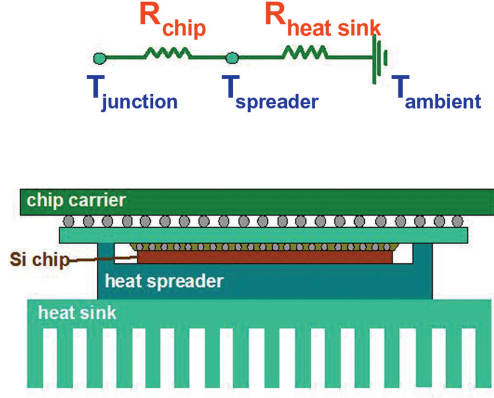


Figure 1.2: schematic diagram of a microprocessor showing its main components, and the abundance of interfaces where heat is generated from *Schelling, Shi, and Goodson (2005)*

perature of the final system by coupling to the external environment. This limits the effectiveness to the efficiency of the coupling between the environment and the integrated circuit. It thus requires the use of heat spreaders, heat pastes, and other metal contacts. However, the heat itself is generated at the nanoscale or at the interfaces between the various components. Hence, in order to better improve heat management of these integrated circuits, we must deal with the issue at the transistor level or at least understand the mechanisms behind heat transfer. Phonons which are the representations of lattice vibrations in solids are the conductors of sound and heat. Low frequency vibrations, smaller than 10^{11} Hz correspond to sound, while higher frequency ones manifest themselves as heat (Figure 1.3). Understanding and controlling phonons is the first step in thermal management and impacting current technology in a way that was achieved by controlling charge and light transport.

Indeed, it is only when we are able to effectively utilize heat through phonons as an energy source, that one of the world's key questions: the dependence on fossil fuels, could also be resolved. In a paper presented to MRS bulletin (*Smalley (2005)*), a possible plan to utilize solar energy was envisioned by placing solar power plants in strategic locations around the Earth. However, as the author indicates, the current state-of-the-art technologies involving solar power do not permit a cost-effective generation of solar-electrical power to meet current energy demands. On the other hand, if we were able to develop solutions to control/stop electron-heat relaxation channels in semiconductors then production of more efficient solar cells can be achieved. In this case, the goal is to reduce the thermal conductivity rather than to increase it as in

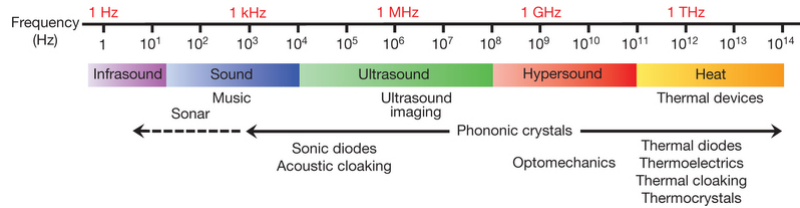


Figure 1.3: Phonon spectrum and its applications. Figure from *Maldovan (2013)*.

the previous cases. *Nevertheless, in this aim we still must be able to understand and control the flow of heat in a semiconductor.*

1.2 Static and transient thermal management

The emergence of the branch of phononics in recent years is the attempt to understand and utilize phonons, the carriers of heat energy in semiconductors, in a beneficial way. One can classify two approaches to this task: the static and the dynamic. The static approach has proven to be useful when it comes to the topic of thermoelectrics, for example. One strategy consists in introducing crystallographic defects, by adding impurities, alloying, or nano-structuring (Iskandar et al. (2015), Pernot et al. (2010), Dresselhaus et al. (2007)). The aim of introducing defects or alloying is to increase the scattering of phonons. The scattering rate will of course depend on the frequency of the phonon-mode, on the temperature, and other factors. These methods are usually employed in thin films of silicon, germanium, aluminium nitride, as well as other semiconductor thin films. Other methods of heat management which involve phonon confinement and localization which are phenomena that manifest themselves in nanostructures and superlattices (Venkatasubramanian (2000), Kim et al. (2006), Balandin and Wang (1998)). Surprising values of the figure of merit ZT have been achieved using these techniques (Suriano et al. (2015), Gunes and Ozenbas (2015), Wu et al. (2014)), and the topic remains an object of active research.

Although static tailoring of the thermal conductivity is of great interest, dynamic control of heat transport can offer interesting scientific and technological applications as well; it may even be unavoidable at times. For example, dynamic heat management can be well suited for systems which are required to adapt to their environment. For example, recent works on developing phonon analogues to the electric diode, transistor, memory, and logic gates (Li et al. (2012)) would allow for applications such as heat-based data storage (Wang and Li (2007)) or "smart" thermoelectric devices which could maximize their efficiency by adjusting their thermal properties to the external temperature. Other examples involve devices which can change their thermal properties depending on a heat load. Component heating in electronic devices, at the end of the day, is dependant on the task load, and such heat loading is essentially of a transient nature. Hence, transient heat management lends itself naturally in this case.

Some of the recent works which approached the idea of transient heat management include thermal rectification, which has been observed experimentally (Kobayashi et al. (2010), Chang et al. (2006)). However, rectification coefficients remain very small for potential integration in applications. Van Zwol et al. (2011) have showed electrically controlled fast nanoscale heat-flux modulation with phase-change materials. They obtained a significant contrast of heat flux due to the interplay between radiation heat transfer at the nanoscale and phase-change materials. Ihlefeld et al. (2015) have experimentally demonstrated for the first time, active and fully reversible control thermal transport in a solid-state device using ferroelectric thin films. Strain has also been used to modify the thermal conductivity dynamically. In a recent study Li et al. (2014) have showed that large reversible changes to thermal conductivity on the order of 70% could be achieved using 2% strain due to the change in the density of

twin-boundaries in thin films. The increase in twin-boundary density has been shown to vary concurrently with the thermal conductivity. [Kulkarni and Zhou \(2007\)](#) have also shown that thermal conductivity can be modified in ZnO nanowires using strain. Under high strain values, above the elastic limit, the phase-change from wurtzite to hexagonal structure induces a change in the thermal conductivity by a factor of almost two. Such effects could be exploited in the development of non-mechanical thermal modulators. Other studies have also shown that strain can be effective in affecting the thermal transport in nanostructures ([Li et al. \(2010a\)](#)) and bulk crystals ([Parrish et al. \(2014\)](#)). *Our motivation for this work is to try and see whether it is possible to modify the thermal conductivity of a piezoelectric material using an electric field through strain.*

1.2.0.1 The thermal switch

A prototype model for a mechanical thermal switch device was presented in [Cho et al. \(2008\)](#). The device is based on two contacts as seen in Figure 1.4 where they are brought closer together by mechanical actuation. The presence of a high-thermal conductivity material in between the substrates or leads changes the thermal resistivity of the device once the two contacts touch. [Cho et al. \(2008\)](#) tested several different

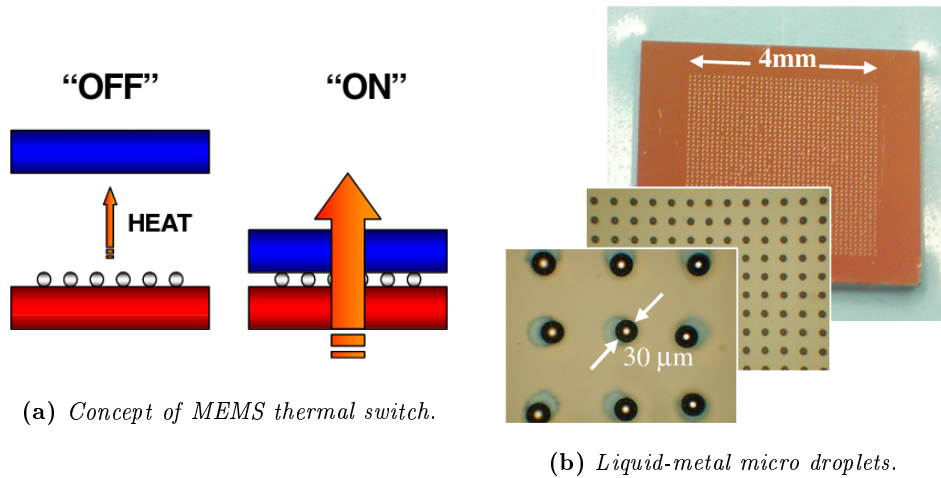


Figure 1.4: A MEMS thermal switch schematic and real-life counterpart. Adapted from [Cho et al. \(2008\)](#)

designs of the contacts such as: silicon-Hg, CNT-Si, CNT-Au-Si, and CNT-CNT. They concluded that the designs based on liquid-metal droplets-based had superior on/off ratio than carbon nanotube based ones. The CNT based switches had high thermal resistance between the CNTs and the other contacts. Hence, their on/off ratios were low. The on/off ratio of the liquid-metal based switch; on the other hand, was roughly 1:100. The applicability of such a switch into a circuit or device is however not discussed. Although Such MEMS devices have high efficiencies when it comes to on/off ratios they do suffer from size disadvantages and from operational degradation..

Other models for thermal switches come from recent works into the effect of strain on thermal conductivity. These works show the possibility of modifying thermal conductivity by mechanical strain. One of the first work which showed the piezo-thermal conductivity in semiconductors was reported by [Keyes and Sladek \(1962\)](#). For low temperatures it was reported antimony-doped Ge crystals showed a large increase in their thermal conductivity when $\langle 111 \rangle$ or $\langle 110 \rangle$ tensile strain is applied. The theory of scattering of phonons by donors predicted the magnitude and effect of applying strain which modified the electrons bands of the antimony donors in the crystal. More recently, [Alam et al. \(2012\)](#) used free-standing amorphous silicon nitride thin films to this end. The authors used films which were 50 nm thick, and the whole device (actuator and sample are a few hundred micrometers large as seen in Figure 1.5. By coupling the film to a MEMS actuator they were able to apply large tensile strains to the films, up to 2.4%. They observed in their experiments that the thermal conductivity decreases with tensile strain, and that the decrease can be up to a factor of almost 8. The authors attributed this decrease to the strong localization of phonon modes in amorphous structures which is not present in crystalline solids. The trend reported in this study differs markedly from experimental measurements performed by [Ftouni \(2015\)](#), who studied thermal transport in SiN_x membranes by coupling the 3ω method to the Völklein geometry and observed that residual stress has no effect neither on the specific heat nor on thermal conductivity.

In a more recent paper [Alam et al. \(2015\)](#) have also shown that the thermal conductivity of 200nm amorphous SiN_x can be *increased* upon mechanical loading up to 2.5%. This contrasting result to the previous experiment was explained by the authors through possible changes in microstructure and/or carrier density. In all cases, we can see that the topic of affecting thermal conductivity using mechanical strain exhibits significant variability and promise. This opens up large possibilities for study and experimentation to build a device such as the thermal switch.

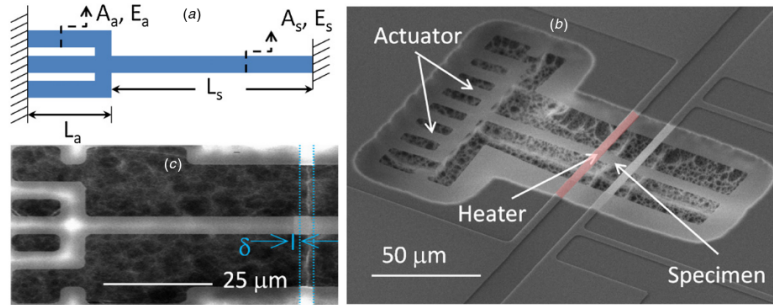


Figure 1.5: (a) Figure showing the single layer SiN three-strip actuator, (b) Scanning electron micrograph of a specimen, (c) Strain is measured post-experiment fracture of the specimen. Adapted from [Alam et al. \(2015\)](#).

As a theoretical "ideal" component our thermal switch is a device that should have dynamic thermal conductivity. When the switch is in the "on" state the heat flow is nominal; the component is a good conductor of heat. In the "off" state the component has a low thermal conductivity, and acts as an insulator. The switch can be triggered by applying strain to the crystal. In the case of a piezoelectric material this strain can

be applied using an external electric field. It would also need to have a fast dynamic time and an high on/off ratio to be efficient. Possible candidates for this application are zinc oxide and aluminium nitride because they exhibit high thermal conductivities and high piezoelectric coefficients.

1.3 Physical background behind solid-state switches

We will now review the necessary physical concepts behind solid-state switches such as lattice vibrations, phonons, thermal conductivity, elastic behaviour of solids, and piezoelectric phenomenon. We will begin by a brief review of the model of thermal conductivity in solids. Since ZnO and AlN are binary compounds and their unit cells contain four atoms, we will use a 1D linear chain in the harmonic lattice approximation. This will help present the phonon-mode properties of wurtzite crystals along the c-axis which may be considered as a linear chain. Next, we introduce the notions of stress and strain, the elastic behaviour in solids. It is also important to elucidate the connection between strain and thermal conductivity. We will also present the phenomenon of piezoelectricity. Finally, we will also discuss some of the general properties of ZnO and AlN, and explain why they are the best candidate materials.

1.3.1 Lattice vibrations

The topic of lattice vibrations whether addressed with a classical or quantum treatment is the first chapter in any book on solid-state physics. For the following discussion we will use the former treatment adapted from [Srivastava \(1990\)](#).

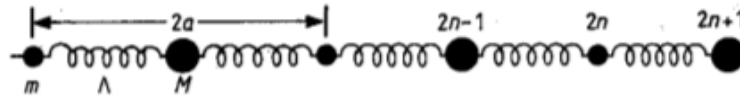


Figure 1.6: A two-atomic linear chain with lattice constant $2a$ and masses m and M ($m < M$) at the equilibrium position from [Srivastava \(1990\)](#)

In most solid materials (crystalline), atoms or molecules are arranged in a regular array of sites, or points in a three-dimensional space, which is known as the crystal lattice. A crystal structure describes a highly ordered structure, occurring due to the intrinsic nature of molecules to form symmetric patterns. At any finite temperature, atoms vibrate about their equilibrium positions. Under the classical approximations, those atom motions can be mathematically described by the Newton's second law if the force applied on each atom and the atomic mass are known.

If we take the linear atomic chain shown in Fig. 1.6, and we assume only nearest-neighbour interactions, we can write the equations of motion for the $2n$ and $2n+1$

atoms equations 1.1 and 1.2

$$m \frac{d^2 u_{2n}}{dt^2} = \Lambda (u_{2n+1} + u_{2n-1} - 2u_{2n}) \quad (1.1)$$

$$M \frac{d^2 u_{2n+1}}{dt^2} = \Lambda (u_{2n+2} + u_{2n} - 2u_{2n+1}) \quad (1.2)$$

Λ is the 2nd order force constant derived from the interaction potential equation 1.3

$$\Phi(u) = \Phi_0 + \underbrace{\frac{1}{2!} \sum_{nk} u_n u_k \frac{\partial^2 \Phi}{\partial u_n \partial u_k}}_{\Lambda_{nk}} + \frac{1}{3!} \sum_{nkl} u_n u_k u_l \frac{\partial^3 \Phi}{\partial u_n \partial u_k \partial u_l} + \dots \quad (1.3)$$

If try solutions 1.4 and 1.5

$$u_{2n} = A_1 \exp i(2nqa - \omega t) \quad (1.4)$$

$$u_{2n+1} = A_2 \exp i((2n+1)qa - \omega t) \quad (1.5)$$

Then equations 1.1 and 1.1 are transformed into the coupled eigenvalue equations equations 1.6 and 1.7

$$-\omega^2 m A_1 = \Lambda [A_2 e^{iqa} + A_2 e^{-iqa} - 2A_1] \quad (1.6)$$

$$-\omega^2 M A_2 = \Lambda [A_1 e^{iqa} + A_1 e^{-iqa} - 2A_2] \quad (1.7)$$

This leads to the matrix equation

$$\omega^2 A_i = \sum_{j=1}^2 D_{ij} A_j \quad i = 1, 2 \quad (1.8)$$

where D_{ij} is the dynamical matrix which contains the elastic coefficient Λ and the masses m, M given by

$$D = \begin{pmatrix} 2\Lambda/m & -(2\Lambda/m)\cos qa \\ -(2\Lambda/M)\cos qa & 2\Lambda/M \end{pmatrix} \quad (1.9)$$

This leads to the secular equation 1.10

$$|D_{ij} - \omega^2 \delta_{ij}| = 0 \quad (1.10)$$

Solving equation 1.10 gives the dispersion relation relating the frequency ω to the wavevector q of the phonon mode equation 1.11.

$$\omega^2 = \Lambda \left(\frac{1}{m} + \frac{1}{M} \right) \pm \Lambda \left[\left(\frac{1}{m} + \frac{1}{M} \right)^2 - \frac{4}{mM} \sin^2 qa \right]^{1/2} \quad (1.11)$$

Equation 1.11 is plotted in figure 1.7. The maximum frequency is known as the Debye frequency. The Debye temperature is related to it using the relation $\theta_D = \hbar\omega/k_B$. Figure 1.7 shows two branches. The top branch is the optical branch, and the lower one is the acoustic branch. The optical branch describes the displacement of the atoms in the primitive or conventional cell. They describe motions of the atoms in opposite

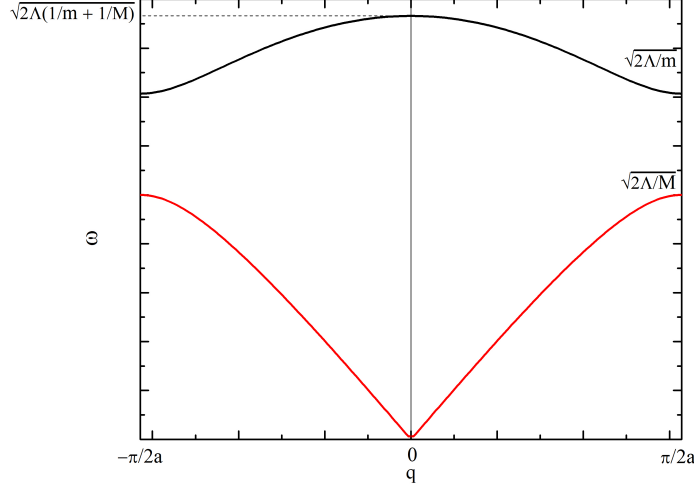


Figure 1.7: *Dispersion relation for linear diatomic chain.*

directions. Therefore, if the two atoms have opposite charges, these modes would be excited by an electric field of the appropriate frequency. The frequencies of said electric fields correspond to the infrared part of the light spectrum. Hence, the name optical branch. The acoustic branch, on the other hand, corresponds to the in-phase motions of the atoms. This is characteristic of a sound wave. Close the Γ point $qa \ll 1$ the dispersion relation described by Eq. 1.11 can be simplified by considering the relationships $\sin x \approx x$ and $\sqrt{1-x} = 1 - \frac{1}{2}x$ when $x \ll 1$ to give equation 1.12

$$\omega^2 \approx \frac{\Lambda}{2(m+M)} q^2 a^2 \quad (1.12)$$

Equation 1.12 provides a linear dependence of frequency on q for the acoustic branch which means a constant group velocity for the acoustical phonons which is known as the sound velocity in materials. These long wavelength modes are also called elastic waves, and can be studied through the application of the wave equation. Such a treatment would see the solid as a continuum rather than a discrete set of particles.

For a one-dimensional linear diatomic chain we see that we have two branches. For the case of a three-dimensional chain, the number of branches will be 6 or $D \times N$ where D is the dimensionality and N is the number of atoms in the unit cell (primitive or otherwise). Among the DN branches, D branches will be acoustical branches and $DN - D$ will be optical. Acoustical branches contribute more to heat conduction because of their higher group velocity, as we shall see in the next section. However, optical modes also play a major roles in phonon-phonon scattering indirectly.

1.3.2 Typical thermal conductivities of semiconductors

The application of a temperature gradient ΔT across a solid results in the excitation of elementary particles such as free electrons, holes, and phonons which acquire more energy than the average or zero-point energy, and transfer heat from the hotter to the colder part of the specimen [Srivastava \(1990\)](#), p.122. In the quantum picture of the coupled harmonic oscillators, which we will not discuss, the energy levels are quantized $E_n = (\frac{1}{2} + n) \hbar\omega$ where $n = 0, \pm 1, \pm 2, \dots, \pm \frac{N}{2}$, where N is the number of atoms. $\frac{1}{2}\hbar\omega$ is the zero point energy of a quantum harmonic oscillator. In addition, the Hamiltonian can be diagonalized and has the form seen in equation [1.13](#)

$$\mathbf{H} = \sum_q \sum_{s=1}^3 \hbar\omega_{q,s} (b_{q,s}^\dagger b_{q,s} + 1/2) \quad (1.13)$$

Where it can be shown that $b_{q,s}^\dagger, b_{q,s}$ respectively create and destroy one *excitation* of energy $\hbar\omega$. These *excitations* are phonons. From this viewpoint, phonons can be regarded as quasi-particles which obey Bose-Einstein statistics, and the Boltzmann equation approach can be applied to them in order to study thermal transport in solids. The general form for the Boltzmann equation for phonons in the steady state of heat-flow is given in equation [1.14](#)

$$-\mathbf{c}_s \cdot \nabla T \frac{\partial n_{\mathbf{q}s}}{\partial T} + \left. \frac{\partial n_{\mathbf{q}s}}{\partial t} \right|_{\text{scatt}} = 0 \quad (1.14)$$

Where $n_{\mathbf{q}s}$ is the distribution function $n_{\mathbf{q}s}(\mathbf{r}, t)$ which measures the occupation number of phonons in mode $(\mathbf{q}s)$, where s is the polarization, in the neighborhood of \mathbf{r} at time t . T is the temperature, and $\mathbf{c}_s(\mathbf{q})$ is the group velocity of mode $\mathbf{q}s$.

In the absence of a temperature gradient $n_{\mathbf{q}s}$ is given by the Bose-Einstein distribution [Eq.1.15](#)

$$\bar{n}_{\mathbf{q}s} := \bar{n}(\omega, T) = \frac{1}{\exp \frac{\hbar\omega(\mathbf{q}s)}{kT} - 1} \quad (1.15)$$

In the presence of a temperature gradient the phonon distribution is spatially non-homogeneous which leads to a rate of change of the distribution function, as described by equation [1.14](#), due to two mechanisms: diffusion and scattering; which in the case of steady state must cancel out. Generally, equation [1.14](#) cannot be solved because it is very complicated as it requires knowledge of the distribution function $n_{\mathbf{q}s}$ for all possible states qs as well as the transition rates from state qs to $q's'$ [Srivastava \(1990\)](#). Therefore, equation [1.14](#) is simplified using the relaxation time approximation [Eq.1.16](#)

$$\frac{\partial n_{\mathbf{q}s}}{\partial t} = -\frac{n_{\mathbf{q}s} - \bar{n}_{\mathbf{q}s}}{\tau_{\mathbf{q}s}} \quad (1.16)$$

Where $\tau_{\mathbf{q}s}$ represents the relaxation time associated with phonon $\mathbf{q}s$ decaying to the average BE distribution. The combination of equation [1.16](#) with assumption of spatial homogeneity (small temperature gradient) leads to the linearized Boltzmann equation

Eq. 1.17

$$-\mathbf{c}_s(\mathbf{q}) \cdot \nabla T \frac{\partial n_{\mathbf{q}s}^-}{\partial T} = \frac{n_{\mathbf{q}s} - \bar{n}_{\mathbf{q}s}}{\tau_{\mathbf{q}s}} \quad (1.17)$$

What is important to us is the relaxation time $\tau_{\mathbf{q}s}$ which is associated with different scattering mechanisms of phonon-scattering such as: mass defect scattering, boundary scattering, dislocation scattering, phonon-electron scattering, and phonon-phonon scattering to name some of the more dominant ones. The scattering rates are dependent on the phonon-mode $\mathbf{q}s$ and on temperature. In the next section we will discuss some of them, and see how they affect thermal conductivity; paying some attention to strain scattering.

Lattice thermal conductivity For a solid subjected to a temperature gradient, Fourier's law describes the rate of energy flow per unit area normal to the temperature gradient (macroscopic expression) Eq.1.18:

$$\mathbf{q} = -\kappa \nabla T \quad (1.18)$$

where κ is the thermal conductivity. The expression for the heat current in a solid is obtained by adding the contribution of all phonons:

$$\mathbf{q} = \frac{1}{N_0 \Sigma} \sum_{\mathbf{q}s} \hbar \omega(\mathbf{q}s) n_{\mathbf{q}s} \mathbf{c}_s(\mathbf{q}) \quad (1.19)$$

Naturally, the thermal conductivity will then depend on the solution of the Boltzmann equation which in turn depends on the expression for the relaxation time. There are several different levels of sophistication to describing phonon relaxation processes through the associated relaxation time. The simplest of which is the single-mode relaxation time approximation (*smrt*) which assumes that one calculates the relaxation rate of phonons in mode $\mathbf{q}s$ under the assumption that all other phonon modes have their equilibrium distribution. What is also important is that the inverse of the total smrt $\tau_{\mathbf{q}s}$ can be expressed as a sum of contributions from all the different scattering mechanisms (Srivastava (1990)):

$$\tau_{\mathbf{q}s}^{-1} = \tau_{\mathbf{q}s}^{-1}(bs) + \tau_{\mathbf{q}s}^{-1}(md) + \tau_{\mathbf{q}s}^{-1}(pp) \quad (1.20)$$

where *bs*, *md*, *pp* stand for boundary scattering, mass-defect, and phonon-phonon, respectively.

Along with the smrt approximation there are other approximations to simplifying the expression for the thermal conductivity which lead/correspond to different models such as the Klemens model (Klemens (1951)), the Callaway model (Callaway (1959), Holland (1963)), and the Srivastava model (Srivastava (1990), p.134). Avoiding any extended comparison or detailed explanation of these models, they can, eventually, all be expressed in the form of the kinetic theory expression (Eq. 1.21)

$$\kappa = \frac{1}{3} C_V \bar{v}^2 \bar{\tau} \quad (1.21)$$

Where C_V is the phonon specific heat defined as $C_V = C/V$ where C is the heat capacity of the solid (at high temperatures it is equal to $3Nk_B$). \bar{v} and $\bar{\tau}$ are average phonon speed and average phonon relaxation time which depend on the particular model.

A graph showing the variation of the thermal conductivity of some typical metals and nonmetals is shown in Figure 1.8.

At low temperatures (well below θ_D) the thermal conductivity of nonmetals such as Si and quartz follows a T^3 . This is related to the heat capacity of the solid which from the Debye model changes as T^3 . More so at low temperatures it can be verified within the *smrt* model that longitudinal phonons contribute only about 10-25% of the total thermal conductivity of semiconductors and insulators while most of the heat is carried by the transverse phonon modes (Srivastava (1990), p.235). At high temperatures anharmonic scattering is the predominant scattering mechanism, and the thermal conductivity will usually follows a T^{-1} behaviour due to that. However, stronger than a T^{-1} has been observed experimentally. The stronger dependence can be satisfactorily explained by including the effect of thermal expansion which makes the elastic constants and as such the Gruneisen coefficients temperature dependent (Srivastava (1990), p.239). This is a first insight into the effect of strain on thermal conductivity. Acousto-optical scattering also plays a big part at high temperatures. For temperatures in-between it is the predominance of defects limiting the mean-free path of phonons.

The effect of strain on thermal conductivity of non-metals One relevant scattering mechanism that we would like to discuss briefly is strain scattering of phonons. The relaxation time associated with elastic strain field scattering of phonons has been studied by Carruthers (1959) using second-order perturbation theory. It was found by the author that the Fourier component of the strain field plays a similar role to that of the potential. This is not unexpected as phonons can be regarded as lattice vibrations or localized strains. The application of the theory to edge dislocations at low temperature shows that the scattering rate is proportional to the density of dislocations σ and to the wavevector magnitude q . Carruthers (1959) also determined a Boltzmann-like equation for the change in the phonon distribution n_{qs} due to the interaction of phonons with the strain field. The results for such a procedure are valid for simple crystals with 1 atom per unit cell or for complex crystals at low temperatures.

1.4 Piezoelectric crystals

In three dimensions there are 219 space groups, and 32 point groups. A crystal will belong to one of these space groups, and to its corresponding point group. The symmetry of the point group will determine the minimum symmetry of the material properties of the crystal such as its elastic constants, its thermal conductivity, or its dielectric constant. For example, for cubic crystals, face-centered, body centered, or simple, the three main directions: [100] [010] and [001] are indistinguishable. Hence, the thermal conductivity $\kappa_{[100]}, \kappa_{[010]}, \kappa_{[001]}$, and the elastic constants C_{11}, C_{22}, C_{33} are

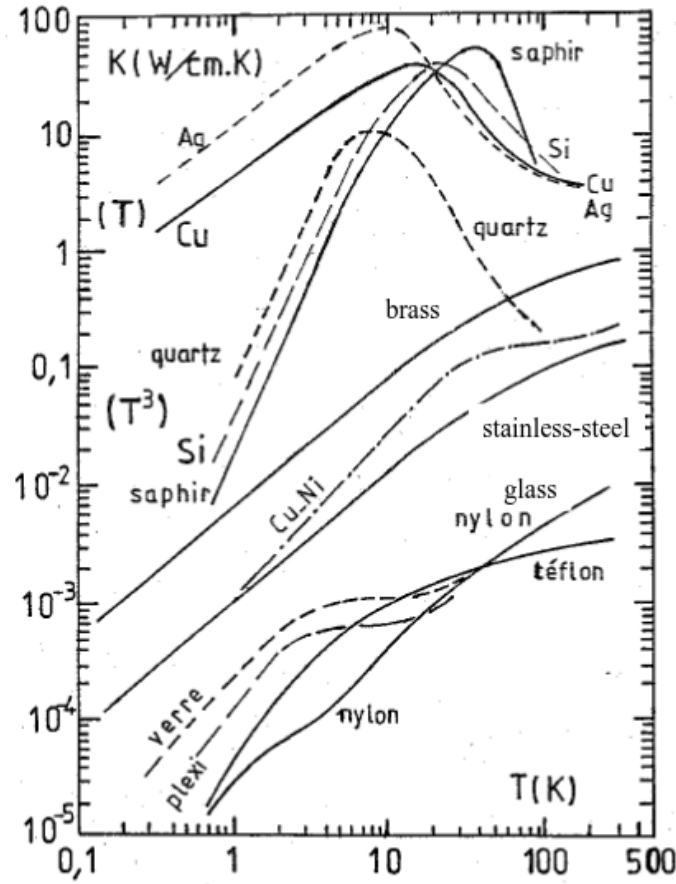


Figure 1.8: Thermal conductivity as a function of temperature for some typical materials.

equal. This is the most important principle in Crystal Physics called Neumann's Principle [Newnham \(2005\)](#). A property which also depends on the symmetry of the crystal is piezoelectricity. The piezoelectric effect was discovered in 1880 by Pierre Curie and Jacques Curie. In certain crystals the application of stress (usually uniaxial) will result in a non-vanishing macroscopic electric polarization field P_i . The coefficient of proportionality is the direct piezoelectric coefficient d_{ijk} eq 1.22. The converse-piezoelectric effect relates the strain τ_{ij} to the external electric field E_i . From thermodynamic arguments it is shown that the two effects have the same coefficient. The units of d_{ijk} are [C/N] or [m/V], which are equivalent. The inverse-piezoelectric effect $e_{ijk} = d_{ijk}^{-1}$ simply inverts the relations in eq 1.22. It is used in the creation of ultrasonic surface waves.

$$\begin{aligned} P_i &= d_{ijk} \sigma_{jk} \\ \tau_{ij} &= d_{ijk} E_k \end{aligned} \tag{1.22}$$

Some typical values of d_{ijk} are shown in fig 1.9.

Table 12.3 Piezoelectric strain coefficients in pC/N

Cubic ($\bar{4}3m$)	d_{14}				
Bi ₁₂ SiO ₂₀	40				
NaClO ₃	1.7				
GaAs	2.6				
ZnS	3.2				
Hexagonal ($6mm$)	d_{31}	d_{33}	d_{15}		
ZnO	-5.0	12.4	-8.3		
CdS	-5.2	10.3	-14.0		
AlN	-2.0	5.0	4.0		
Tetragonal ($4mm$)	d_{31}	d_{33}	d_{15}		
BaTiO ₃	-34.5	85.6	392		
PbTiO ₃	-25	117	62		
Tetragonal ($\bar{4}2m$)	d_{14}	d_{36}			
KH ₂ PO ₄	1.3	21			
NH ₄ H ₂ PO ₄	1.8	48			
Tetragonal (422)	d_{14}				
TeO ₂	8.1				
Trigonal ($3m$)	d_{31}	d_{22}	d_{33}	d_{15}	
LiNbO ₃	-1.0	21	16	74	
LiTaO ₃	-3.0	9.0	9.0	26	
Tourmaline	-0.3	-0.3	-1.8	-3.6	
Trigonal (32)	d_{11}	d_{14}			
α -Quartz	2.3	-0.67			
Orthorhombic (222)	d_{14}	d_{25}	d_{36}		
Rochelle salt	2300	-56	12		
Orthorhombic ($mm2$)	d_{31}	d_{32}	d_{33}	d_{15}	d_{24}
PbNb ₂ O ₆	-43	24	60	180	170
Poled ceramics (∞m)	d_{31}	d_{33}	d_{15}		
BaTiO ₃	-78	190	260		
Pb(Zr, Ti)O ₃					
PZT-5H	-274	593	741		
PZT-8	-27	225	330		
K _{0.5} Na _{0.5} NbO ₃	-51	127	306		

Figure 1.9: Values of piezoelectric constants for some typical materials from *Newnham (2005)*

For the 32 point groups in three dimensions, 21 are piezoelectric. Of the remaining 11, 9 are centrosymmetric: they possess a center of inversion. Centrosymmetry forbids the presence of the piezoelectric effect. ZnO and AlN both belong to the ($6mm$) point group or the wurtzite crystals structure $P6_3mc$ space group. The piezoelectric effect manifests in that structure due to the displacement of the ions from their equilibrium lattice positions. This leads to a non-vanishing polarization. The structure has 3

independent piezoelectric coefficients

$$\begin{pmatrix} P_1 \\ P_2 \\ P_3 \end{pmatrix} = \begin{pmatrix} 0 & 0 & 0 & 0 & d_{15} & 0 \\ 0 & 0 & 0 & d_{15} & 0 & 0 \\ d_{31} & d_{31} & d_{33} & 0 & 0 & 0 \end{pmatrix} \begin{pmatrix} \tau_1 \\ \tau_2 \\ \tau_3 \\ \tau_4 \\ \tau_5 \\ \tau_6 \end{pmatrix} \quad (1.23)$$

ZnO has the largest piezoelectric coefficient d_{33} of all binary semiconductors. Therefore, it will exhibit the largest strain for a set electric field value. Typical dielectric breakdown fields for most materials are around 1-10 MV/m; that translates to 0.1-10 MPa stress or 0.001-0.01% strain for ZnO and AlN.

1.5 Organization of the thesis

In chapter 2 we will introduce the numerical methods used to study the effect of strain on thermal conductivity. This mainly includes non-equilibrium and equilibrium molecular dynamics simulations (NEMD and EMD). We will introduce the inter-atomic potentials used for the simulation of different materials.

In chapter 3 we show the results concerning the effect of uniaxial strain on the thermal conductivity of bulk ZnO and AlN crystals. We apply mechanical strain ranging between -6% and 6%. We demonstrate that the dependence of thermal conductivity on strain follows a power law. We also study the size effect on the calculation of the thermal conductivity using NEMD for ZnO and AlN, and show that it is independent from the value of the strain applied. We also show evidence of the modification of the thermal conductivity of ZnO using an external electric field. For AlN we show that the thermal conductivity is not affected by compressive or tensile strain for the values proposed.

In chapter 4 we study the effect of local non-uniform strain on the thermal conductance of superlattices of Si/Ge, SiO₂/C, and ZnO/C. We use non-equilibrium molecular dynamics to show that in Si/Ge superlattices local in-plane and cross-plane strain at the interfaces leads to the same drop of thermal conductance. The effect of an external electric field on the thermal conductances of SiO₂/C and ZnO/C superlattices is studied using EMD and NEMD. We show that it is only for the case of SiO₂/C superlattices that a local strain can be applied, and that such strain leads to reduction of the thermal conductance. For ZnOC superlattices, on the other hand, no modification of the conductance is seen. The results for SiO₂/C show promise for applications in piezothermal devices.

Finally, we conclude the thesis by reviewing the major results, and by indicating the work that is still required to validate them.

Chapter 2

Molecular Dynamics

2.1 Introduction

”Une intelligence qui, pour un instant donné, connaîtrait toutes les forces dont la nature est animé, et la situation respective des êtres qui la composent (...) rien ne serait incertain pour elle, et l’avenir comme le passé, serait présent à ses yeux.”

— Pierre Simon Laplace, *Essai Philosophique*

Molecular dynamics is a powerful tool for calculating the static and transport properties for a range of systems; gas, solid, and liquid. It has been applied to a number of important and difficult problems involving protein folding, crack propagation in solids, and non-newtonian flows. The power of MD is providing detailed atomic level information that is necessary and unavailable in other methods which use continuum modelling. Historically, MD was used mainly for liquids; as solids and gases already had well established theories such as the kinetic theory and the Debye model for simple crystals at a range of temperatures. These models are well suited for describing solids and liquids at thermal equilibrium

MD simulations can have an important role in bridging the gap between theory and experiment. They can provide a way to obtain useful information about a system of interest before investing time and effort. Apart from some of their limitations, MD simulations do not remove the anharmonicities of the atomic interactions. Even though the interactions are not as 'accurate' as ab initio based methods they can still reproduce many interesting macroscopic properties that have to do with phonon transport such as thermal expansion, thermal conductivity, and some interesting phase transitions. The computational costs of MD vary depending on the size of the system, and the complexity of the inter-atomic potential. Typically, systems from a few hundred up to a few million atoms are possible to simulate using MD, and potentials can include two-body, three-body, and other effects.

In the following, we will discuss the requirements to building a MD simulation, its limitations and relevant quantities that can be obtained by applying statistical anal-

ysis. This development will serve as a background to the later derivations of thermal conductivities and piezoelectric coefficients in chapters three and four.

2.2 Physical principles of Molecular Dynamics

2.2.1 Equations of Motion

As shown in Eqs. 2.1, MD simulations begin by the time integration of Newton's equations of motion for each atom which are considered as a classical point masses. The forces between the atoms are set by the derivatives of the interaction potential. Figure 2.1 represents typical features of a MD cell. The unit cell represents the unit cell of the solid. This can be the conventional or primitive cell defined for the crystal structure. The unit cell as defined here needs to recreate the periodic crystal structure when tiled along the three directions X,Y, and Z. The supercell represents the cutoff radius of the inter-atomic potential. In Figure 2.1 it shows that the simulation takes into account with first and second neighbor interactions of each atom. It is important for the final size of the domain to be twice as large as the cutoff distance to avoid any self-interaction effects. We can also see that in this representation we have two different atom types, and boundary conditions. When an atom crosses a periodic boundary it is remapped back into the simulation domain rather than being lost. With periodic boundary conditions the atoms across the boundaries are interacting; hence, periodic-boundary conditions simulate bulk structures.

After initialization the positions and momenta of the atoms are allowed to evolve according to the classical equations of motion. For N atoms we have $6N$ equations. Without other constraints the equations will represent a single phase trajectory of the system in microcanonical ensemble. The number of atoms, volume, and energy are conserved (NVE). The canonical ensemble (NVT) can be simulated by the addition of a Nosé-Hover thermostat Hoover (1985). This is done by the addition of an extra equation to the set of $6N$ equations. MD simulations, in general, are deterministic and time-reversible.

$$\begin{aligned}
 m_1 \frac{d^2 \mathbf{r}_1}{dt^2} &= \mathbf{F}_1 \\
 m_2 \frac{d^2 \mathbf{r}_2}{dt^2} &= \mathbf{F}_2 \\
 &\vdots \\
 m_N \frac{d^2 \mathbf{r}_N}{dt^2} &= \mathbf{F}_N
 \end{aligned} \tag{2.1}$$

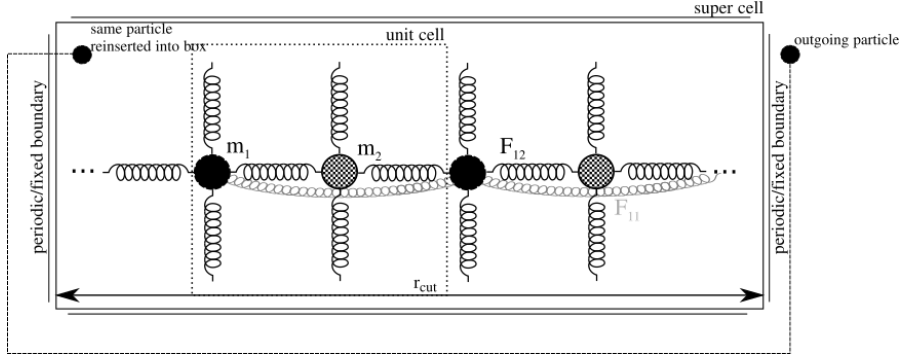


Figure 2.1: Representation of the basic element of a MD cell where atoms are interacting through potential forces. Periodic boundary conditions are used to induce a translational symmetry and mimic an infinite size system.

where, taking $\Phi(r_{ij})$ as the interatomic potential function

$$\mathbf{F}(i) = \sum_{j \neq i} \mathbf{F}_{ij} = - \sum_{j \neq i} \frac{\partial \Phi(r_{ij})}{\partial \mathbf{r}_{ij}} \quad (2.2)$$

Here m_i is the mass of atom i , \mathbf{r}_i refer to the position of atom i . \mathbf{F}_i is the force on atom i due to all its neighbours. The derivatives are calculated analytically from the interaction pseudopotential Φ . Examples of which are reported in Table 2.1.

2.2.2 Solving the equation of motion

Two initial conditions are required for each atomic trajectory to be calculated -as indicated by the second time-derivative term in the motion equation-, therefore initial *positions* and *velocities* for each atom should be set in the first place. When crystals are to be computed, the positions are set by the crystal lattice. Unfortunately, the length scales involved in MD are on the order of a few hundreds of nanometers. Hence, structures such as polycrystalline solids or thick interfaces cannot be fully resolved due to computational limitations. Nano-structures, on the other hand, are perfectly suited for MD. Velocities can be randomly drawn according to a Maxwellian distribution including the desired temperature, but a white noise distribution might also be relevant as its relaxation to the Maxwellian distribution is reached within fewer atomic periods.

Then a numerical scheme allows for calculating the atomic trajectories, the simplest numerical scheme being:

$$\begin{aligned} \mathbf{p}(i, t + \Delta t) &= \mathbf{p}(i, t) + \mathbf{F}(i, t) \Delta t \\ \mathbf{r}(i, t + \Delta t) &= \mathbf{r}(i, t) + \mathbf{p}(i, t + \Delta t) \Delta t / m_i \end{aligned}$$

Potential Name	Functional form $\Phi(r_{ij})$	Relevant materials
Buckingham	$A \exp(-r/\rho) - \frac{C}{r^6}$	SiO, ZnO, MgO (oxides, ionic compounds)
Lennard-Jones	$A/r^{12} - B/r^6$	Argon, graphene
Morse	$D [(1 - \exp(-a(r - r_0)))^2 - 1]$	ZnO, NaH (diatomic molecules)
Coulombic	$-q_i q_j / r$	ionic compounds

Table 2.1: *List of common MD potentials used in this work*

Here Δt is the timestep, $\mathbf{p}(i)$ is the momentum of atom i . $\mathbf{F}(i)$ is the force on atom i due to all its neighbours. Note that the large toolbox of numerical techniques for integrating differential equations is currently used in the standard online codes typically including high-order Runge-Kutta and Verlet algorithms. The timestep is chosen such that $1/\Delta t$ is larger than the maximum vibrational frequency in the system. For ZnO, this frequency lies around 18 THz and around 20 THz for Si, which corresponds to a period of 55 fs. Hence, a timestep of 1 fs would ensure a reasonable resolution of all atomic vibrations and conservation of the total energy with fluctuations on the order of 0.001%.

The initial state of the system should not have an influence on the measurement of macroscopic quantities that is to be made, which is the case once the chosen initial coordinates describe the chosen statistical ensemble and are averaged either over a sufficient duration or over a large enough number of trajectories.

Once the initial state is set and the system is allowed to evolve, thermal equilibrium has to be reached. Due to their different orders, different macroscopic quantities, such as temperature, pressure, heat flux, strain..., relax to their equilibrium values on different timescales. While temperatures are converging as quickly as one atomic period at equilibrium, several nanoseconds might be required for the heat fluxes to reach the relevant regime.

As the rms fluctuation amplitude of temperature is reversely proportional to the square root of the number of samples, averaging over more timesteps might also be needed for small systems. Thermal equilibrium can finally be confirmed by the convergence of the temperature integrated over time or by checking that the distribution of the velocities is Maxwellian-like.

2.2.3 Forces

The inter-atomic forces are perhaps the most challenging aspect of a MD simulation. They are set using available models from the literature and have to be chosen according to the quantities to be estimated. The features of the force field are especially crucial to describe the thermal conductivity. The Boltzmann description of this latter quantity

is in an integral over the phonon modes:

$$\kappa_L = \frac{1}{3} \int \hbar \omega_q v_g^2 \tau_q \frac{\partial N_q^0}{\partial T} D(q) dq \quad (2.3)$$

where the density of states $D(q)$ and the frequencies versus wave-vectors appear and are specific to a given solid crystal, depending on the crystal lattice and the inter-atomic potential. The selected potential will have to provide the accurate phonon dispersion curves and density of states.

2.2.3.0.1 Potential for ZnO For oxides, and more specifically for ZnO, most studies use the Van Beest, Kramer, and van Santen (BKS) potential. The BKS potential is a two-body potential which was originally developed in 1990 for silica and aluminophosphate polymorphs (van Beest et al. (1990)). It takes the following form

$$\Phi_{ij} = \frac{q_i q_j}{r_{ij}} + A_{ij} e^{-r_{ij}/\rho_{ij}} - \frac{C_{ij}}{r_{ij}^6} \quad (2.4)$$

The first term describes point-charge interaction. This is usually the most computationally demanding portion of the potential since it is slow to converge, and will only do so under certain conditions. Ewald summation (Ewald (1921)) is usually employed to handle the long range nature of this coulombic interaction. The problem with coulombic interactions which have a r^{-1} form is that they are unbounded; therefore, they require special computational techniques. However, less computationally methods such as the cell-multipole (Ding et al. (1992)) and Wolf method (Wolf et al. (1999)) also exist, and have been shown to reproduce the general dynamics and energies of Ewald summed systems (Fennell and Gezelter (2006)). The value q_i will be close to that of the formal charge of the atom i . Empirical fittings of the potential might however cause deviations from the conventional charge values.

The remaining terms form what is known as the Buckingham potential. The first term describes repulsion at short range due to the overlap of closed electron shells (Pauli type repulsion). It replaces the r^{12} repulsion term in the well-known Lennard-Jones potential. The A and ρ parameters are in units of energy and distance respectively. The latter of which should be used to determine the required cut-off value for the potential. In van Beest's et al original paper these two parameters for the ij species were obtained by fitting the potential to ab initio data.

Finally, the last term is the well-known London dispersive term, and was originally fitted using bulk rather than ab initio data. However, the term also has a well-established physical meaning J. (1994) and maybe calculated using the Slater-Kirkwood formula Slater and Kirkwood (1931) as was done for the case of ZnO.

Although this potential has a relatively simple form, for example, it does not contain any three-body terms, it has supplied, rather successfully, several important features of silica such as the the transition temperature of quartz, the unit cell parameters,

Species	A (eV)	ρ (Å)	C (eV.Å ⁻⁶)
O ²⁻ -O ²⁻	9547.96	0.21916	32.0
Zn ²⁺ -O ²⁻	529.70	0.3581	0.0
Zn ²⁺ -Zn ²⁺	0.0	0.0	0.0

Table 2.2: Coefficients for inter-atomic potential representing ZnO

elastic constants [van Beest et al. \(1990\)](#), and piezoelectric constants [Herzbach et al. \(2005\)](#) close to experimental values. Hence, the validity of the potential over a range of pressure values and over a number of different silica polymorphs made this functional form attractive for use in molecular dynamics simulations. Van Beest's paper specifies that the potential could be applied to "... any other chemical elements that form tetrahedral network oxides..." [van Beest et al. \(1990\)](#). However, there still exists certain discrepancies when using this potential. For example, a recent paper has shown the advantage of other potentials incorporating extra degrees of freedom, and it has displayed the shortcomings of the BKS potential [Herzbach et al. \(2005\)](#) when it comes to fundamental quantities such as the vibrational density of states. Therefore, extensions to the potential and even modifications are providing better accuracy. For example, one may extend the potential by a shell model which aims at modeling the polarizability of an atom using an additional degree of freedom represented by a massless particle harmonically coupled to the ionic core [Herzbach et al. \(2005\)](#). Another closely related potential to the BKS potential was proposed by Vashishta et al. It adds steric repulsion, Debye screening, charge-dipole interaction, and three-body terms to the functional form and has been applied to several materials including SiO, SiC, and AlN [Vashishta et al. \(1990\)](#), [Vashishta et al. \(2007\)](#), [Vashishta et al. \(2011\)](#).

2.2.3.1 Validation of inter-atomic model for ZnO

The wurtzite zinc oxide crystal belongs to the P6₃mc space group - hexagonal lattice. [J. \(1994\)](#) provided an empirical fit of the BKS potential for the case of ZnO using the lattice energy, cell parameters, and elastic constants for several structures. This fit done under a shell model, but the results should be equally valid for the point ion model. In fact, the Binks parametrization of the BKS potential both using the shell and core-only versions have been used in several MD simulations of ZnO; more specifically to study the piezoelectric properties of ZnO [Momeni et al. \(2012\)](#), [Kulkarni and Zhou \(2006\)](#), [Dai et al. \(2010\)](#). The Binks coefficients for ZnO are given in Table 2.2

We first calculate the density of states for a perfect ZnO crystal using the velocity autocorrelation function. The initial cell parameters are $a=3.265$, $c=5.155$, and $u=0.3882$. We start with 15 unit cells in each direction, apply periodic boundary conditions and relax the system in an NPT ensemble for 10000 timesteps (timestep 1éfs). After which we obtain the vibrational density of states by taking the Fourier transform of the velocity autocorrelation. We compare our results with ab initio data from [Serrano \(2004\)](#). We use here the GULP code [Gale and Rohl \(2003\)](#) to calculate the phonon density of states and dispersion curves.

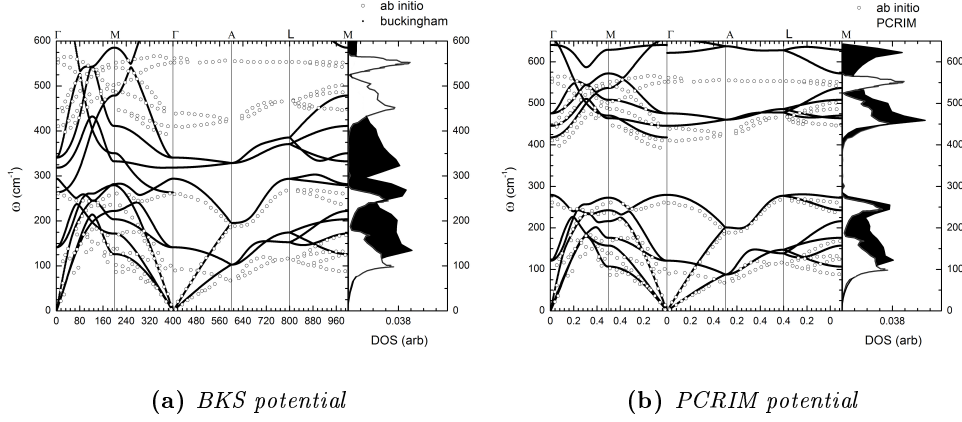


Figure 2.2: Comparison of dispersion relations and vibrational density of states for ZnO calculated using MD and lattice statistics at 0K. The white points/curve represents the *ab initio* data, and the dark lines/curve represent our calculating using MD for the DOS and lattice dynamics for the dispersion curves.

We also present the dispersion curves along several symmetry directions and compare them to *ab initio* data also obtained from [Serrano \(2004\)](#). The data was calculated using the code GULP for the same potential (core-only) and cell parameters used in the MD runs. Ewald summation was used in both the lattice dynamics and molecular dynamics simulations to calculate the long-range forces.

We note in both instances the large differences between *ab initio* calculated phonon states and those calculated using the BKS potential. Nevertheless, the BKS potential is actually able to reproduce many of the bulk properties of ZnO such as the elastic, piezoelectric, and the static dielectric constants. The elastic constants are usually used as fitting parameters and as such it is no surprise that the potential reproduces them as seen in Table 2.3. It should of course be noted that the elastic constants are related to the acoustic modes of the crystal which as we can see in Figure 3 are satisfactorily well reproduced. The longitudinal optical modes on the other hand are poorly recreated as well as the high frequency oxygen modes. Hence, the Binks potential should be used with care. Any (non static) optical of thermal properties calculated will inevitably suffer from large deviations from experimental values.

2.2.3.1.1 PCRM potential for MD simulation of ZnO A recent improvement to the Binks parameterization of the BKS potential was given in [Wang et al. \(2014\)](#). There, the functional form of the potential was chosen based on the lattice inversion method, and was then empirically improved (fitted). The model used in the paper is the partially charged rigid ion model (PCRM) and corresponds to a combination of the BKS and Morse potential. It has the functional form given in equations 2.5 and 2.6

$$\Phi(r_{ij}) = Ae^{-r_{ij}/\rho} \quad (2.5)$$

	This Work (BKS-no shell)	This work (PCRIM)	Tu and Hu (2006)	Kobiakov (1980)
a (Å)	3.2706	3.238	3.199	
c (Å)	5.1379	5.176	5.167	
u (Å)	0.3891	0.381	0.379	
c ₁₁	232.6	221.2	218	210
c ₁₂	95.3	119.8	137	118
c ₁₃	85.6	97.2	121	106
c ₃₃	210.6	222.8	229	210
c ₄₄	74.6	51.17	38	45
Method	LD	LD	DFT	Exp

Table 2.3: Comparison of the lattice parameters and elastic constants of ZnO obtained using different methods.

Species	Type	A(eV)	ρ (Å)	C (Å ⁻¹)	q
Zn-Zn	Eq.2.5	78.91	0.5177		+1.14
Zn-O	Eq.2.5	257600	0.1396		
O-O	Eq.2.6	0.1567	3.405	1.164	-1.14

Table 2.4: Parameters for the PCRIM potential for ZnO. Taken from Wang et al. (2014).

For Zn-O and Zn-Zn interaction

$$\Phi(r_{ij}) = A[(1 - e^{-C(r_{ij}-\rho)})^2 - 1] \quad (2.6)$$

For O-O interactions The potential parameters are given in Table 2.4

For further details on the derivation of the potential one should consult Wang et al. (2014). Here we just present the phonon dispersion relations and density of states using this potential (Fig.2.2b). We can see the substantial improvement in the agreement between the LD and ab initio data when using this potential. Hence, it will be the potential used for the simulation of ZnO.

2.2.3.2 Vashishta potential for AlN

For MD simulation of AlN there exists in literature two inter-atomic potentials: a Tersoff based potential Tungare et al. (2011), and a potential based on a combination of 2-body and 3-body forces including a modified Stillinger-Weber type potential steric-size effects, screened Coulomb interactions, charge-induced dipole, and van der Waals interactions which we shall refer to as the Vashishta potential (Vashishta et al. (2011)). The Tersoff based potential has shown good agreement between the experimental and calculated values of AlN thermal expansion coefficient, bulk modulus, and lattice parameters. However, it lacks electrostatic forces which are necessary for the simulation of the piezoelectric and dielectric properties of AlN. On the other hand, the Vashishta potential has been shown to reproduce the correct phonon-mode density of states as

well as the elastic coefficients, lattice cohesive energy, and elastic constants. It has also reproduced the pressure-induced phase change of AlN from wurtzite to rock-salt at high pressure and temperature (3000K, 25GPa), and has reproduced some features of the AlN amorphous structure specifically the phonon-mode density of states. Unfortunately, the Vashishta potential is not included in the LAMMPS code package. Hence, we had to modify the code to include this potential which is given in

$$\Phi = \sum_{i < j} \Phi_{ij}^{(2)}(r_{ij}) + \sum_{i, j < k} \Phi_{jik}^{(3)}(r_{ij}, r_{ik}) \quad (2.7)$$

Where

$$\Phi_{ij}^{(2)}(r_{ij}) = \frac{H_{ij}}{r_{ij}^{\eta_{ij}}} + \frac{Z_i Z_j}{r_{ij}} e^{-r/\lambda_{ij}} - \frac{D_{ij}}{r^4} e^{-r/\xi_{ij}} - \frac{W_{ij}}{r_{ij}^6} \quad (2.8)$$

$$\Phi_{jik}^{(3)}(r_{ij}, r_{ik}) = B_{jik} \exp\left(\frac{\gamma}{r_{ij} - r_0} + \frac{\gamma}{r_{ik} - r_0}\right) \frac{(\cos\theta_{jik} - \cos\bar{\theta}_{jik})^2}{1 + C_{jik} (\cos\theta_{jik} - \cos\bar{\theta}_{jik})^2} \quad (2.9)$$

Where $\Phi_{jik}^{(3)}(r_{ij}, r_{ik}) = 0$ for r_{ij} or $r_{ik} > r_0$. The coefficients for the potential are given in Figure 2.3

TABLE II. Parameters for two-body and three-body terms of the interaction potential used in the MD simulation of AlN.

		Z_i (e)	λ (Å)	ξ (Å)	r_c (Å)	e (C)
Two-body	Al	1.0708	5.0	3.75	7.60	1.602×10^{-19}
	N	-1.0708				
		η_{ij}	H_{ij} (eV Å ^{η})	D_{ij} (eV Å ⁴)	W_{ij} (eV Å ⁶)	
Two-body	Al-Al	7	507.668 6	0	0	
	Al-N	9	367.055 46	24.7978	34.583 65	
	N-N	7	1038.163 34	49.5956	0	
		B_{jik} (eV)	$\bar{\theta}_{jik}$ (deg)	C_{jik}	γ (Å)	r_0 (Å)
Three-body	Al-N-Al	2.1536	109.47	20	1.0	2.60
	N-Al-N	2.1536	109.47	20	1.0	2.60

Figure 2.3: Parameters for the Vashishta potential for AlN taken from [Vashishta et al. \(2011\)](#)

To also verify the correctness of the integration of the potential into LAMMPS we have calculated the vibrational density of states using molecular dynamics by using the velocity autocorrelation function. We have compared our calculation to that found in [Vashishta et al. \(2011\)](#). The good agreement between the two graphs in Figure 2.4

indicates that the potential has been successfully integrated into LAMMPS, and that we can proceed with the calculation of other properties of AlN.

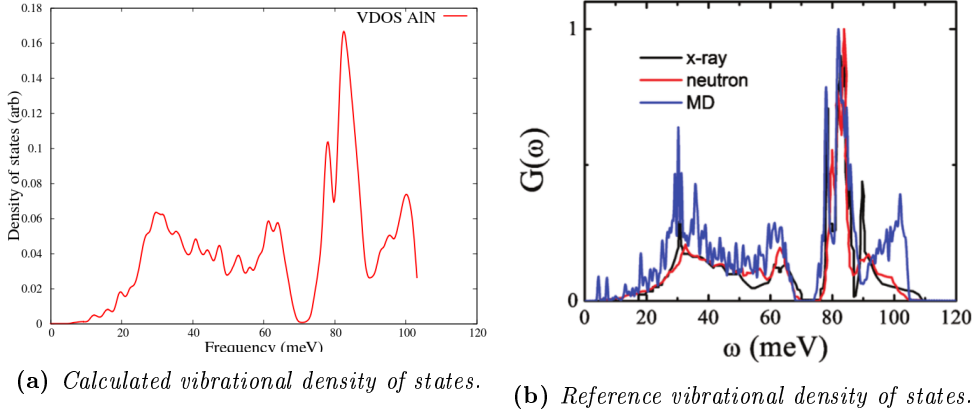


Figure 2.4: Comparison of the vibrational density of states of AlN calculated using MD and the Vashishta potential to the one found in [Vashishta et al. \(2011\)](#).

2.3 Thermal and mechanical macroscopic quantities

Macroscopic quantities can be derived from the microscopic trajectories as reported in Table 2.5. The definition of temperature intrinsically relies on the assumption of equilibrium or local equilibrium so that the canonical average of the kinetic energy can be set equal to its microcanonical average. This equality yields to the temperature as a function of atomic velocities and masses.

The expression of the pressure also involves local equilibrium as it includes the thermal contribution and is set by the Virial theorem. This latter theorem indeed relates the average kinetic and potential energies to temperature [Greiner \(2001\)](#).

The heat flux expression is directly derived from the steady state heat conduction equation when replacing the heat flux by its microcanonical expression [Volz \(2009\)](#). These standard formulas are implemented in the code used [Plimpton \(1995\)](#).

2.3.1 Thermal Conductivity from Equilibrium Molecular Dynamics Simulation

Equilibrium molecular dynamics simulations -which consists in constraint free trajectory computations- allows us to implement the fluctuation-dissipation theorem from linear response theory which relies in the connection between the energy dissipation in irreversible processes and the thermal fluctuations in equilibrium [Kubo et al. \(1985\)](#). As reported above, the net flow of heat in a solid, given by the heat current vector \mathbf{J} , fluctuates around zero at equilibrium. In the Green-Kubo (GK) method, thermal

Quantity	Formula
Temperature	$\frac{\sum m_i v_i^2}{3Nk}$
Pressure	$\frac{Nk_B T}{V} + \frac{1}{3V} \sum_i^{N-1} \sum_{j>i}^N r_{ij} \cdot F_{ij}$
Heat flux	$\mathbf{J} = \frac{1}{V} \sum_{i<j} (\mathbf{f}_{ij} \cdot \mathbf{v}_j) \mathbf{r}_{ij}$

Table 2.5: Formulas for thermal and mechanical quantities calculated during a MD simulation. k refers to the Boltzmann constant and N to the number of kinetic degrees of freedom.

conductivity is related to the integral of the autocorrelation of those fluctuations. In the case of an isotropic material, the conductivity is defined by [Kubo et al. \(1985\)](#)

$$\kappa = \frac{1}{k_B V T^2} \int_0^\infty \langle J_x(t) J_x(0) \rangle = \frac{1}{3k_B V T^2} \int_0^\infty \langle J(t) \cdot J(0) \rangle \quad (2.10)$$

where V represents the volume of the simulation cell, t is the time, $J_x(t)J_x(0)$ and $J(t) \cdot J(0)$ are the heat current autocorrelation functions (HCACF) in the x direction and all directions, respectively. In crystals where the fluctuations have long life-times (and long phonon mean free paths), the HCACF decays slowly. The thermal conductivity being related to the integral of the HCACF is accordingly large. In materials such as amorphous solids, where the mean free path of phonons is small, thermal fluctuations are quickly damped, leading to a small integral of the HCACF and a low thermal conductivity [McGaughey and Kaviany \(2004\)](#).

In real computational procedures, instead of integrating up to infinity in Eq. 2.10, the upper limit is a finite but long enough time period that captures the correct statistics. The continuous integral is also replaced by a discrete summation. To remove the arbitrariness on the choice of the upper limit, different methods have been proposed in the literatures [Volz et al. \(1996\)](#); [Che et al. \(2000\)](#); [McGaughey and Kaviany \(2004\)](#); [Li et al. \(1998\)](#). According to the Cattaneo-Vernotte's relation [Vernotte \(1958\)](#); [Cattaneo \(1958\)](#), Volz et al derived the time autocorrelation function of the heat flux as [Volz et al. \(1996\)](#)

$$\langle \mathbf{J}(t) \cdot \mathbf{J}(0) \rangle = \langle \mathbf{J}(0) \cdot \mathbf{J}(0) \rangle \exp(-t/\tau) \quad (2.11)$$

A similar exponential function was used by Li et al to fit the heat flux autocorrelation function

$$\frac{\langle \mathbf{J}(t) \cdot \mathbf{J}(0) \rangle}{3} = g \exp(-t/\tau) \quad (2.12)$$

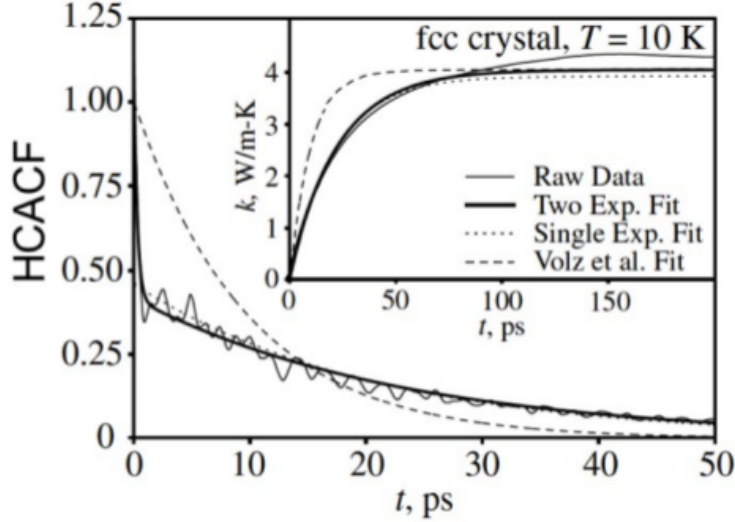


Figure 2.5: An example of heat flux autocorrelation function with the fitting of different methods. The insert represents the integral of the thermal conductivities over time. Figure from McGaughey and Kaviani (2004)

However, in Li's approach, the single exponential function is not used to fit the whole HCACF curve but only the range $[t_1, t_2]$. This approach is used to determine the tail contribution of HCACF. Instead of using a single exponential function to fit the HCACF in the full time interval, Che et al. (2000) proposed a double exponential function to fit the whole HCACF curve. This approach has also been used by McGaughey et al. (2004) for solid Ar but with different explanations. The fitting function reads as

$$\frac{\langle \mathbf{J}(t) \cdot \mathbf{J}(0) \rangle}{3} = A_{sh} \exp(-t/\tau_{sh}) + A_{lg} \exp(-t/\tau_{lg}) \quad (2.13)$$

where the subscripts sh , and lg refer to short range and long range, respectively. Fig. 2.5 shows an example of HCACF obtained from solid Ar at 10 K and the corresponding fitting curves with Eq. 2.11, 2.12 and 2.13.

2.3.2 Thermal Conductivity from Non-equilibrium Molecular Dynamics Simulation

Non-equilibrium molecular dynamics, also known as the direct method, extracts the thermal conductivity from the Fourier's law. In this method, a one-dimensional temperature gradient is imposed on a simulation cell by allowing thermal power exchange

between the heat source and sink while measuring the resulting heat flux. The thermal conductivity is then obtained as the ratio of the heat flux to the temperature gradient. An alternative, but equivalent way consists in inducing a heat flux and to measure the resulting temperature gradient. In both cases the system is first allowed to reach a steady state, after which long simulations are conducted allowing to obtain correct statistical measurements. The NEMD method is often the method of choice for studies of nanomaterials while for bulk thermal conductivity, particularly highly conductive materials, the equilibrium method is typically preferred due to less severe size effects [Termentzidis and Merabia \(2012\)](#).

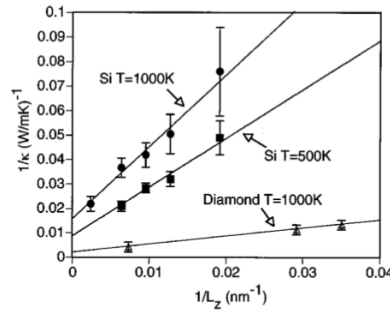


Figure 2.6: The inverse of the thermal conductivities measured with NEMD simulations for Si and diamond at specified temperatures versus $1/L$ and the corresponding fitting with Eq. 2.15. κ_∞ is get at $1/L = 0$. Figure from Schelling et al (2002), *Phys. Rev. B* 65: 144306

In NEMD simulations, finite-size effects arise when the length of the simulation cell L is not significantly longer than the phonon mean free path. This is understood to be a result of scattering that occurs at the interfaces with the heat source and sink. As a result, the phonon mean free path is limited by the system size. To eliminate the size effect, Schelling et al [Schelling et al. \(2002\)](#) proposed a method based on the Matthiessen's rule to determine the effective mean free path Λ_{eff} when $L \sim \Lambda_\infty$, where Λ_∞ is the mean free path for an infinite system. The effective mean free path is obtained by the following relation:

$$\frac{1}{\Lambda_{eff}} = \frac{1}{\Lambda_\infty} + \frac{4}{L} \quad (2.14)$$

Here, the factor of 4 accounts for the fact that as phonons travel along the length of the simulation cell from the source to the sink, its average distance since the last scattering event should be $L/4$. In kinetic theory, the thermal conductivity is given as $\kappa = \frac{1}{3}C_v v \Lambda$, where C_v and v are the specific heat and the phonon group velocity. Combing with Eq. 2.14, the effective thermal conductivity is obtained:

$$\frac{1}{\kappa_{eff}} = \frac{1}{\kappa_\infty} + \frac{12}{C_v v} \frac{1}{L} \quad (2.15)$$

Eq. 2.15 suggests that a plot of $1/\kappa$ vs $1/L$ should be linear, and that the thermal conductivity of an infinite system can be obtained by extrapolating to $1/L = 0$. Fig. 2.6 shows the examples of using Eq. 2.15 to extract the thermal conductivity with infinite sizes for Si and diamond. Good linear fits are found in these cases imply the successful application of Eq. 2.15.

2.4 Physical limitations and conclusions

Molecular Dynamics has been widely used to predict various properties in bulk and nanomaterials. It has been regarded as a successful tool to assist the experimental designs and understand the mechanisms at the atomic scales. Despite its applications, it also suffers from several important and fundamental challenges.

Limitations of MD modeling are related first to the absence of electron kinetic. Electronic properties of materials cannot be simulated and the free electron contribution to thermal conductivity is therefore not accounted for. For semiconductors such as AlN and ZnO this is not an issue as the main contribution to heat conduction is provided by atomic vibrations.

The second limitation holds in the fact that simulations involve only classical solids. MD simulations are therefore supposed to be valid for solids above the Debye temperature θ_D . The average phonon mode occupation number is proportional to temperature according to $\langle n(\omega_{\mathbf{q}}) \rangle = kT/\hbar\omega$; and the heat capacity follows Dulong-Petit law. Note that this limitation does however not exclude phonon confinement and rarefaction effects. On a general basis, a less restrictive criteria than the Debye temperature is applied and MD is usually assumed to be relevant to temperatures down to one third of the Debye temperature. This criteria in fact applies in the cases where low frequencies mainly drive the behaviours of macroscopic quantities.

In the next chapters, the behaviour of the simulated materials will be mainly governed by atomic vibrations rather than by electron motions and the simulation temperatures will remain larger than room temperature so that deviations to the Bose-Einstein distribution will be considered as negligible.

Chapter 3

Origin of thermal conductivity changes in bulk material. Effect of uniaxial strain

In this chapter we will investigate the effect of uniaxial strain on the thermal conductivity of bulk perfect crystals. We begin each section with a short introduction to the current available data on the thermal conductivity of bulk crystals then we proceed with the results of our calculations. The thermal conductivity of ZnO and AlN crystals has been calculated using the NEMD method 2.3.2. Uniaxial strain has been applied to perfect ZnO and AlN crystals either by remapping atom coordinates with a change in simulation-box length, or by applying a static electric field. The strain, thermal conductivity, and electric field have all been calculated/applied parallel to the c-axis of the crystals since ZnO and AlN crystals have the highest values of piezoelectric constant and thermal conductivity along this direction. The objective is to quantify the effect of strain on the thermal conductivity, and find the largest possible change of thermal conductivity for a static electric field before dielectric breakdown.

3.1 Description of simulation procedure

To determine the equilibrium lattice parameters at zero strain and 300K we run a simple simulation under NPT ensemble for 1 ns. In order to calculate the thermal conductivity of strained ZnO and AlN crystals the following steps describes the procedure in general:

1. *Initialize:*

The atom positions are initialised using the equilibrium lattice parameters $a = 3.2706$, $c = 5.1379$ for ZnO, and $a = 3.112$, $c = 4.0982$ for AlN. Both crystals have the wurtzite which is represented by the lattice vectors and assymetric unit

AB where A is Al or Zn atom, and B is N or O atom:

$$a_1 = \frac{a}{2} \begin{pmatrix} \sqrt{3} \\ -1 \\ 0 \end{pmatrix} \quad a_2 = a \begin{pmatrix} 0 \\ 1 \\ 0 \end{pmatrix} \quad a_3 = c \begin{pmatrix} 0 \\ 0 \\ 1 \end{pmatrix} \quad (3.1)$$

$$B_1 = \begin{pmatrix} 1/3 \\ 2/3 \\ 0.375 \end{pmatrix} \quad B_2 = \begin{pmatrix} 2/3 \\ 1/3 \\ 0.875 \end{pmatrix} \quad A_1 = \begin{pmatrix} 1/3 \\ 2/3 \\ 0 \end{pmatrix} \quad A_2 = \begin{pmatrix} 2/3 \\ 1/3 \\ 0.5 \end{pmatrix} \quad (3.2)$$

The lattice spacing along the X, Y, and Z directions were $\sqrt{3}/2a$, $1.5a$, and $1.0c$ respectively. Periodic boundary conditions are applied across all faces of the simulation domain. The timestep was set to 0.001ps.

2. *Equilibrate:*

A few tens of ps under NPT conditions with $T = T_{eq} = 300K$, $P = 0$ GPa

3. *Apply strain and heat flux:*

The box is scaled along the Z direction by a factor $\epsilon = 1 + \text{strain}$, and the atom positions are rescaled. The rescaling is important as solid deformation is an affine deformation. Alternatively, an electric field is applied to the simulation domain under NPT conditions. The simulation domain is concurrently subdivided into 20 bins along the Z direction, and the velocities of 2 atoms in bins 1 and 11 are exchanged every $t_{mp} = N_{mp} \times \Delta t$ as per the Muller-Plathe algorithm.

4. *Stabilize:*

The system is allowed to reach steady state under NVT conditions. A few hundred ps are usually enough to obtain a linear stable temperature profile as in figure 3.2. It typically takes more time for the system to reach steady state than to equilibrate.

5. *Collect data:*

The heat flux and temperature profile are then sampled every N_{mp} steps, the thermal conductivity calculated (post-processed), and averaged.

3.1.1 Muller-Plathe method

The Muller-Plathe method (MP) is a reverse NEMD method for calculating the thermal conductivity. In NEMD simulations the thermal conductivity is calculated from the macroscopic definition; equation 3.3

$$\kappa_{ij} = \lim_{\frac{dT}{dx_i} \rightarrow 0} \lim_{t \rightarrow \infty} - \frac{\langle q_i(t) \rangle}{\langle dT/dx_i \rangle} \quad (3.3)$$

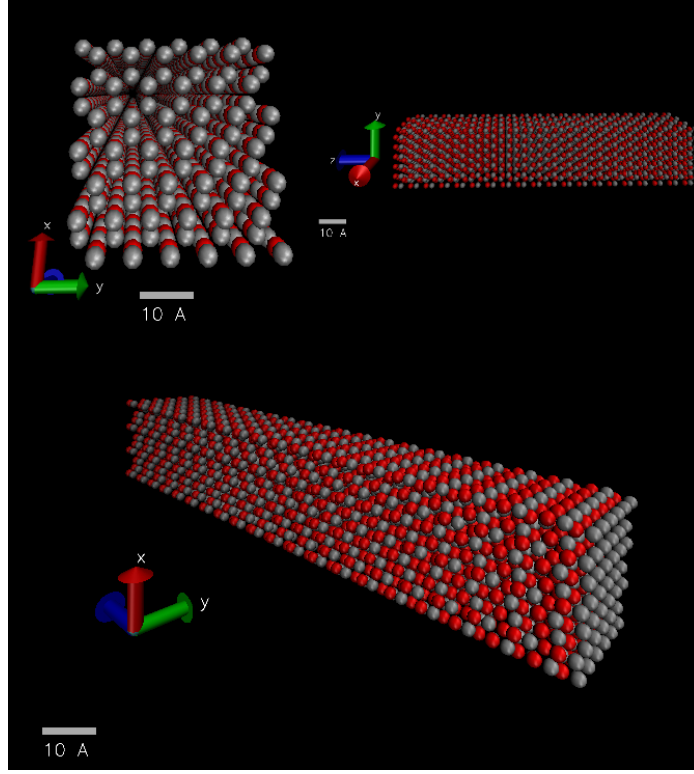


Figure 3.1: Perspective images of $4 \times 8 \times 20$ uc ZnO crystal after initialization. The silver and red atoms represent zinc and oxygen atoms respectively.

The MP method involves applying a heat flux to the system after having reached steady state and calculating the temperature gradient to obtain the thermal conductivity. The method has several advantages over the direct EMD method ([Müller-Plathe \(1997\)](#)) which involves applying a thermal gradient and then calculating the heat flux. For instance, it is well-known that the heat flux is a slow converging quantity; on the other hand, using the MP method it is well-defined. The temperature gradient is faster to converge and faster to calculate, and the magnitude can be controlled by adjusting N_{mp} . Hence, MP method simulations are typically shorter.

The crystal is subdivided into an even number of bins N as in figure 3.3. The first bin is the cold bin and the $N/2 + 1$ bin is the hot bin. At fixed intervals of a fixed number of timesteps, N_{mp} , the hottest atom in the cold bin and the coldest atom in the hot section have their velocities rescaled according to equations 3.4 3.5.

$$\mathbf{v}'^c = -\mathbf{v}^c + 2 \left[\frac{m_c \mathbf{v}^c + m_h \mathbf{v}^h}{m_c + m_h} \right] \quad (3.4)$$

$$\mathbf{v}'^h = -\mathbf{v}^h + 2 \left[\frac{m_c \mathbf{v}^c + m_h \mathbf{v}^h}{m_c + m_h} \right] \quad (3.5)$$

Equations 3.4 and 3.5 enable the exchange of heat between the two bins while conserving the kinetic energy and linear momentum of the system ([Stackhouse and Stixrude](#)

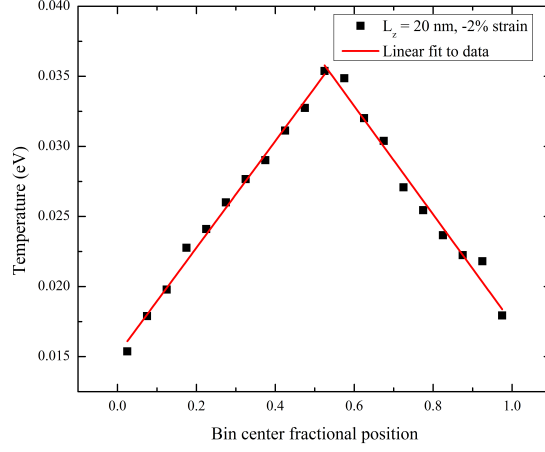


Figure 3.2: A representative temperature profile at 300K, -2% strain after 500ps of applying the Muller-Plathe algorithm.

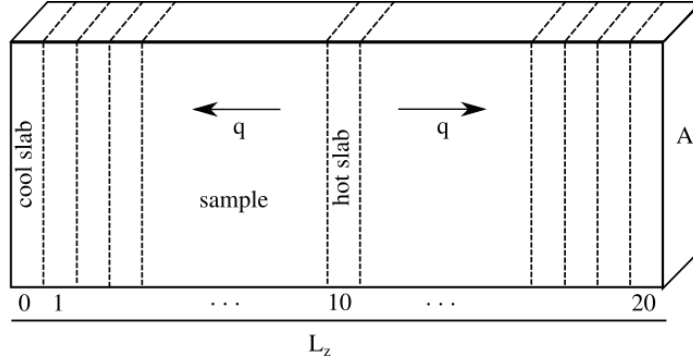


Figure 3.3: Schematic representing the Muller-Plathe algorithm

(2010)). $\mathbf{v}^c, \mathbf{v}^h, m_c, m_h$ are the velocities and masses of the cold and hot atoms respectively. The average heat flux can be calculated directly from the difference of kinetic energies of the hot particle before and after the exchange equation 3.6

$$q_i = \frac{1}{2AN\Delta t} \sum_{\text{transfers}} \frac{1}{2} m_h \left(v_i'^h{}^2 - v_i^h{}^2 \right) \quad (3.6)$$

Where N is the number of elapsed timesteps, Δt is the timestep, A is the area perpendicular to the flow of heat q_i , and $i = x, y, z$. Once steady state is reached the macroscopic equation for thermal conductivity equation $q_i = -\kappa_{ij} dT/dx_j$ is used to calculate the thermal conductivity.

The temperature gradient $\frac{dT}{dx_i}$ is calculated by linearly interpolating the temperatures of each bin, figure 3.2.

3.2 Thermal conductivity of bulk ZnO crystals

3.2.1 Experimental measurements of ZnO thermal conductivity

The bulk thermal conductivity of ZnO has been measured experimentally from 1K to 300K (Wolf and Martin (1973)). The values have been fitted to the Debye-Callaway model eq 3.7, and various averaged phonon properties such as the Gruneisen parameters, sound velocity, and relaxation times for phonon-phonon, boundary, defect, and isotope scattering have been extracted. The expression for the relaxation times is given in equation 3.8.

$$\kappa = \frac{k}{2\pi^2v} \left(\frac{kT}{\hbar} \right)^3 \int_0^{\theta/T} \tau \frac{x^4 e^x}{(e^x - 1)^2} dx \quad (3.7)$$

$$\tau^{-1} = \frac{v}{L} + A\omega^4 + [B_1 \exp(-\theta/aT) + B_2]\omega^2 T + Y\omega \quad (3.8)$$

Two of the three samples in this study were single crystal ZnO hydrothermally grown and lithium doped while the third was vapor grown and undoped. The thermal conductivity was measured using a conventional longitudinal steady-state heat-flow apparatus. The measurements showed that thermal conductivity parallel and perpendicular to the c-axis are not very different, and that at room temperature the doping does not have a significant effect. The measurements were also compared to those of Slack (1972), and found to be in good agreement. Hence, from those measurements the thermal conductivity parallel to the c-axis at room temperature was around 68 W/mK.

On the other hand, the highest, and more recent, thermal conductivity of ZnO reported in literature is around 150 W/mK (Ozgur et al. (2006)). The samples in this study were melt-grown, and were subjected to different thermal treatments. The thermal conductivity in this study was measured using scanning thermal microscopy (SThM). It was noted that the thermal conductivity measured using thermal probe techniques depends on the surface treatment which removes surface defects, and improves the crystal structure at the surface.

As previously stated ZnO belongs to the $P6_3mc$ crystal group. Therefore it has an anisotropic thermal conductivity. However, as shown in the experiments, this anisotropy is small $\kappa_{||c}/\kappa_{\perp c} = 1.13 - 1.15$ (Wolf and Martin (1973)). Therefore, it is sufficient to calculate the thermal conductivity along the c-axis as the perpendicular conductivity will not differ greatly. Hence, we will restrict ourselves to calculating the thermal conductivity parallel to the c-axis of the crystal in our MD simulations.

3.2.2 Molecular Dynamics calculation of ZnO thermal conductivity

Effect of system length To study the effect of the length of the simulation domain on the thermal conductivity we calculated the thermal conductivity for 15, 20, 30, 40, 45 cells in the Z-direction and 7×4 cells cross-section or 19.70×19.5 Å (XY plane). The number of atoms in the simulations was between 2520 and 7560. A full simulation (20 unit cell length) took 1.3 hours to complete using 48 CPUs (Intel Xeon X5650). The PCRM potential for ZnO (Wang et al. (2014)) was used with a cut-off of 6.0 Å. Ewald summation with an accuracy of $1.0E-6$ was used to calculate the long-range forces. The equilibration time was 3ps, followed by 20ps to reach steady state, and 50ps for data sampling. The heat exchange step size was $N_{mp} = 25$ which yielded a temperature profile of $T_{hot} = 390K \pm 20$ and $T_{cold} = 220K \pm 40$ for the 5 simulations.

We have calculated the thermal conductivity parallel to the c-axis as a function of the length of the system in the same direction. We then plot the inverse thermal conductivity versus the inverse system length as seen in Figure 3.4. As we can see from Figure 3.4 increasing the system length leads to an increase of the thermal conductivity. The trend can be well represented by a straight line. This shows that from equation 2.15 we can extract the infinite-length thermal conductivity. Linear regression analysis of the data gives an adjusted R-square of 0.903 and an intercept of 0.0024 ± 0.0003 mK/W. This gives an infinite-length thermal conductivity to be $\kappa_{||c}^{\infty} = 410 \pm 60$ W/mK. This value is representative of a perfect crystal without any defect, impurity, or isotope scattering. Our value and that of the largest reported in literature have a large difference. This disagreement between the absolute values of MD and experimental can be explained by the following arguments:

1. The Debye temperature of ZnO is between 322K and 800K as can be seen in table 3.1.

	θ_D (K)	Source	Reference
1	322	Calculated from average sound velocity $v_s = 3.4 \times 10^5$ cm/s	Wolf and Martin (1973)
2	399	Fitting heat capacity to Debye model at low temperature. The sample contained a high concentrations of defects and impurities	Morkoc and Ozgur (2009), p.58
3	805	Equivalent temperature of the highest phonon-mode frequency at the Γ point for ZnO ($A_1^{LO} = 560$ cm ⁻¹) from ab initio data	Serrano (2004)

Table 3.1: Debye temperature of ZnO at room temperature from different sources available in literature.

2. Second, the experimental data given in Ozgur et al. (2006) which represents the highest value measured in literature were done using surface thermal microscopy. This technique is known to be inadequate to measure highly conductive materials

due to the contribution of the tip-sample contact resistance that predominates if the sample resistance becomes too low.

3. The two thermal conductivities are on the same order of magnitude which is acceptable considering that the potential used in the MD simulation was not fitted taking into account the *thermal* properties of ZnO.

Bearing all this in mind: that an MD simulation represents a perfect, impurity free, infinite length sample, and that no enriched perfect sample data exists for ZnO the value of 416 W/mK can be considered as an upper limit to the possible thermal conductivity of ZnO.

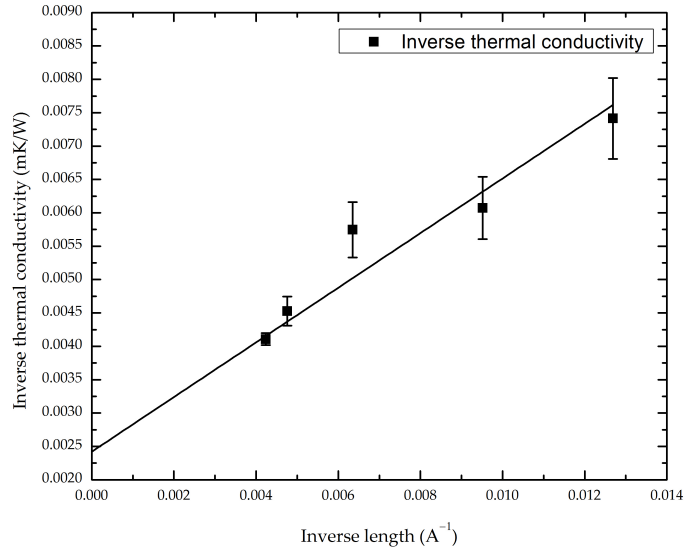


Figure 3.4: *Dependence of thermal conductivity on the length of the MD simulation cell. The thermal conductivity of the infinite system is deduced from the value extrapolated when the reverse of the length goes to zero.*

3.2.3 Effect of uniaxial strain on the thermal conductivity of zinc oxide

There have been studies of the effect of strain on the thermal conductivity of bulk crystals such as argon (Bhowmick and Shenoy (2006)), silicon (Parrish et al. (2014)), and nanostructures such as carbon nanotubes (Chalopin et al. (2012)), silicon nanowires (Li et al. (2010b)), silicon thin films (Xu and Li (2009)), and on interfacial conductance (Abramson AR (2002)), (Shen et al. (2011)). For simple LJ like crystals the thermal conductivity is seen to decrease as a power law going from compressive to tensile stress. The exponent was shown to depend on the Grueneisen parameter and the exponent of the inter-atomic potential (Bhowmick and Shenoy (2006)).

For the simulations involving strained crystals the simulations proceeded in almost the same way as for the non-strained case. The system length was set to $7 \times 6 \times 20$ ZnO unit cells yielding a simulation domain of $19.70 \times 19.5 \times 104$ Å which contains 3360 atoms. We used 50ps for equilibration, 500ps to reach steady-state, and 50ps for data collection. We have used the same random number to initiate the velocities of the atoms for the different strain simulations. This improves the accordance between the values as a function of strain. To calculate the long-range forces we used Wolf summation as it is significantly less costly in terms of computation time.

The strain is applied by resizing the box in the Z-direction and rescaling the atoms. The box volume is then maintained constant for the rest of the simulation. This of course modifies the potential energies of the atoms, and the temperature of the system is seen to increase slightly (about 10%) even for small strains (less than 3%). To remedy this NVT conditions are applied to the simulation domain. The strain is monitored by calculating the domain size in the Z-direction, and comparing it to the non-stressed case. The pressure is also monitored during the data collection period, and in Figure 3.5 we see that the crystal starts to deviate from the elastic behaviour at 4% and -3% strain. The elastic coefficient of ZnO is between 183 and 232 GPa (Sarasamak et al. (2010)[p.9]) which fits well with the value of 202 ± 8 obtained by linear regression from Figure 3.5.

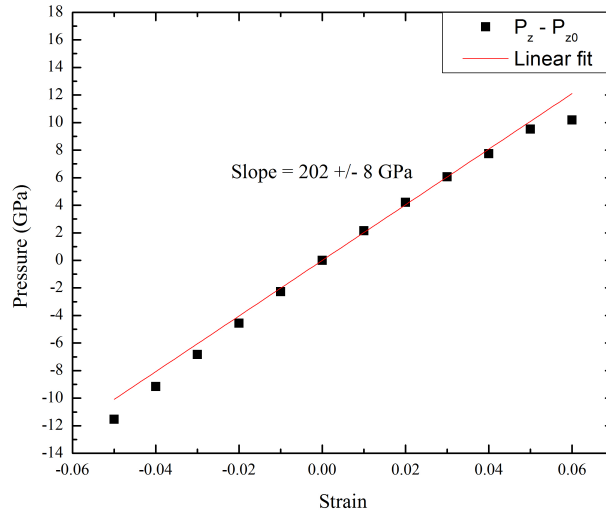


Figure 3.5: Pressure versus strain for $7 \times 4 \times 20$ ZnO crystal at 300K. The strain and pressure are averaged over the data collection period. The straight line represents the linear fit of the data with the intercept fixed at zero.

For all simulations the atom-swap step size is $N_{mp} = 15$, and the temperature gradient is 3.0 ± 0.3 K/Å. From this 33 samples of the temperature gradient, heat flux, pressure, and strain are obtained. The thermal conductivity, pressure are calculated and averaged for each strain value.

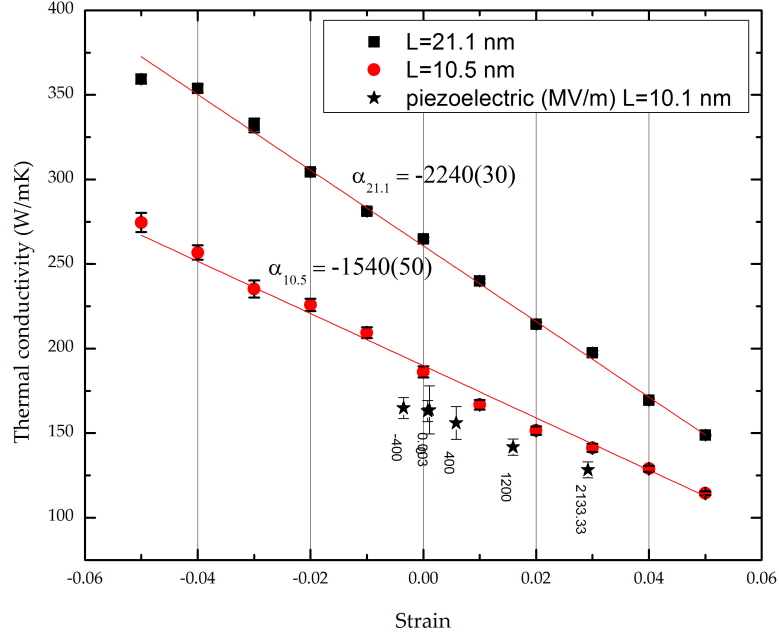


Figure 3.6: *Effect of strain on the thermal conductivity of ZnO bulk crystals*

For ZnO the effect of strain on bulk thermal conductivity has yet to be studied. In Figure 3.6 we show this study for two different lengths of bulk crystals. We see that the thermal conductivity linearly decreases going from compressive to tensile strain as predicted in other studies (Bhowmick and Shenoy (2006)), (Parrish et al. (2014)). However, the coefficient of proportionality is observed to change with the box size. In fact, the coefficient of proportionality α increases by a factor of 1.45 as the system doubles in length. This might be an indication that the strain affects the long-wavelength phonons which are not resolved with a smaller system size. Therefore it is important to correct for the size effect before obtaining the correct coefficient of proportionality. We do this as the next step.

Bhowmick and Shenoy (2006) model for thermal conductivity as a function of strain In a recent work it was shown that strain affects the scattering rate of phonons. Assuming the classical limit of phonon distribution i.e. temperatures above the Debye temperature of a solid, we have that the number of phonons n at temperature T for mode-frequency ω is given by $n \approx k_B T / \hbar \omega$, and by using Fermi's golden rule it was shown that the scattering rate for phonons τ is proportional to the frequency of the phonon-mode ω and to the third order force constants of the lattice Γ . These terms, the frequency and force constants, were in turn shown to be dependent on the strain to some power $\propto \epsilon^{-\gamma}$. The exponent γ can be shown to be a combination of the Grueneisen parameter and inter-atomic potential power (Bhowmick and Shenoy

(2006)). Also, using the kinetic theory $\kappa \propto Cv^2\tau$ and the Debye approximation $v \propto \omega$. It was determined that the thermal conductivity is inversely proportional to the temperature, and decreases as a power-law as a function of strain as noted in equations 3.9 and 3.10.

$$\kappa \propto \frac{1}{T}\epsilon^{-\gamma} \quad (3.9)$$

Where the strain in this case is calculated as

$$\epsilon = V/V_0 \quad (3.10)$$

Where V_0 is the volume of the crystal at zero strain. Therefore, we have corrected our data seen in Figure 3.6 for the size effect seen in Figure 3.4 using equation 3.11.

$$\kappa_{\epsilon,\infty}^{-1} = \kappa_{\epsilon,L_z}^{-1} - \frac{0.403}{(1+\epsilon)L_z} \quad (3.11)$$

Where $\kappa_{\epsilon,\infty}^{-1}$ is the thermal conductivity at a strain ϵ for an infinite length system, κ_{ϵ,L_z} is the thermal conductivity at a strain ϵ at a finite system length (in this case we used the data for $L_z = 21\text{nm}$), L_z is the system length equal to 211\AA , and 0.403 is the slope of the line seen in Figure 3.4.

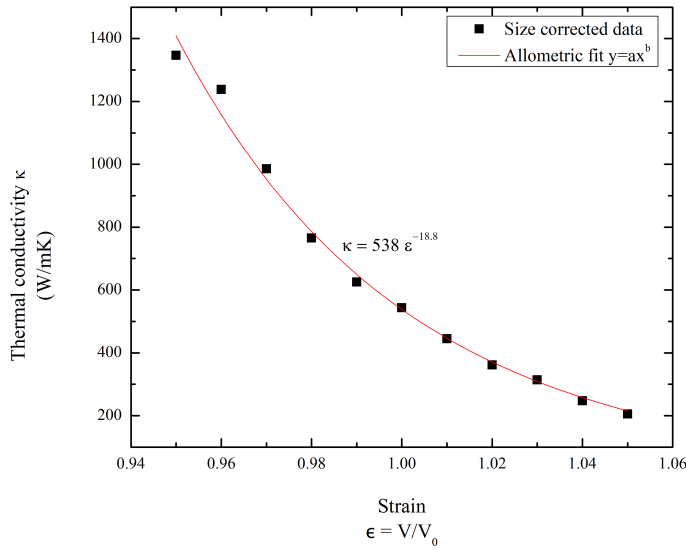


Figure 3.7: Thermal conductivity corrected for size effect as a function of strain at 300K. The red line represents the fitting of the data to a power law function.

We have plotted this data in Figure 3.7 as a function of the strain $\epsilon = V/V_0 = L_{z,0}/L_{z,\epsilon}$. We can see that we do recover the power law dependence for ZnO quite well. The exponent obtained from the fitting is equal to -18.8 ± 0.8 . Therefore, with a typical strain value of 0.01, for example, the percentage change of thermal conductivity can be calculated from $\kappa = 538\epsilon^{-18.8}$ to be -17%. To be able to stretch a ZnO crystal

by 1% along the c-axis we need 2.1 GPa ($C_{33} = 210 \text{ GPa}$) or $E_z = 8.1 \times 10^8 \text{ V/m}$ electric field ($d_{33} = 12 \text{ m/V}$).

3.2.4 Effect of uniaxial strain on phonon properties

Strain modifies the unit cell length and the interatomic distance yielding a modification in phonon eigenfrequencies and force constants. For constants in turn affect group velocities and eigenfrequencies also as shown in Eqs. 3.12.

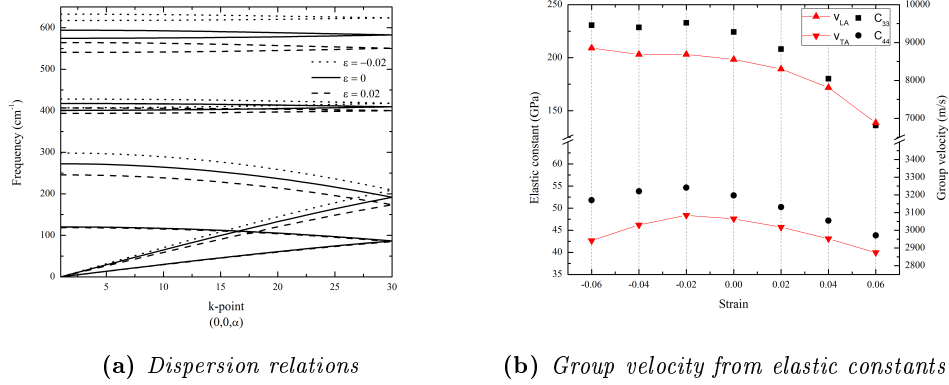


Figure 3.8: Phonon mode properties as a function of strain along the $[0001]$ direction

More specifically, uniaxial compression increases the frequencies and group velocities of the longitudinal phonon modes along the strain direction while tensile strain decreases them. The transverse mode velocities are also increased slightly for moderate strains (less than 0.6). We utilized lattice dynamics calculations at zero temperature and zero pressure using the GULP code. The PCRM potential and the equilibrium lattice constants from the MD simulations were used as input. A $10 \times 10 \times 10$ mesh was then used to calculate the dispersions relations. The GULP code uses the dynamical matrix constructed from the inter-atomic force constants to find the eigenvalues and eigenvectors. To obtain the dispersion relations for the strained structure we simply changed the unit cell parameter. Hence, the lattice parameter for 0, -2%, and 2% strain are 5.245286, 5.14038028, and 5.35019172, respectively. The dispersion relations were calculated along the $\Gamma - A$ direction or in k-vector form $k = [00k_z]$. The behaviours for the dispersion curves seen in other works such as Parrish et al. (2014) are the same for the case of ZnO as we can see in Figure 3.8. The elastic constants were also calculated from lattice dynamics and the group velocities for the TA and LA modes for wurtzite structure Rosen and Klimker (1970) were estimated from them using equation 3.12

$$\begin{aligned} v_{TA}([0001]) &= \sqrt{C_{44}/\rho} \\ v_{LA}([0001]) &= \sqrt{C_{33}/\rho} \end{aligned} \quad (3.12)$$

3.2.5 Piezothermal resistance in ZnO

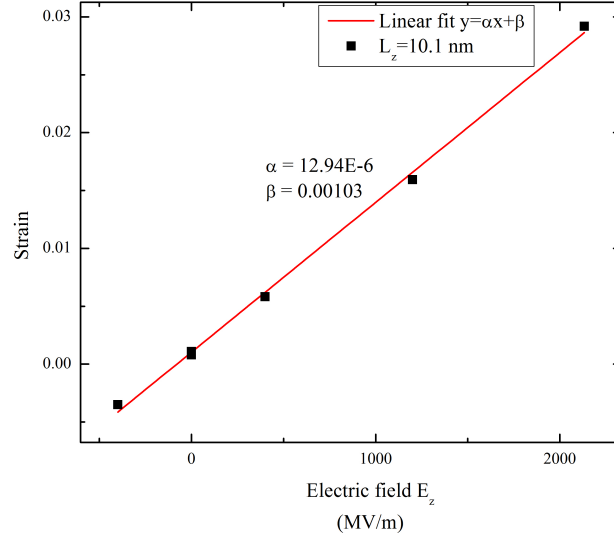


Figure 3.9: Strain versus electric field strength along the c -direction. The straight line represents the linear fit of the data where α is the slope and β is the y -intercept.

In order to investigate possible thermal conductivity alterations through electrical actuation, the impact of electric fields applied to the atomic system was also investigated. For the system length of 10.5 nm, we have applied several static electric fields along the c -axis direction, and calculated the strain and the thermal conductivity. So, instead of changing the box length we apply a static electric field parallel to the Z -direction, and we allow the box to change size by applying NPT conditions. This permits the atoms to adopt their new equilibrium positions due to the additional electrostatic force term $q_i E_z$. The ratio of the induced strain to the electric field magnitude is the piezoelectric coefficient d_{33} . No surface charge redistribution was observed due to the periodic boundary conditions.

In Figure 3.9 we have plotted the strain versus the applied electric field. The strain was calculated by averaging the domain length during the data collection period. We see that the relation between the strain and the applied electric field is linear even for field values up to 2 GV/m. Such large fields would normally induce dielectric breakdown of any material. The breakdown field depends on the bandgap of the material, and also on the size and microstructure. Typical values of the magnitude of breakdown fields are between 1 MV/m and 1 GV/m. This phenomenon is not observed in MD simulations due to the absence of electrons. Nevertheless, it is possible to increase the piezoelectric coefficient of ZnO by nano-structuring. Recent studies using first-principles methods have shown that ZnO nanowires of diameters of 0.6 to 2.4 nm have a giant piezoelectric effect (Agrawal and Espinosa (2011)). This was explained by the surface rearrangement of atoms which reduces the volume of the nanowire compared to a bulk crystal with the same number of atoms. Since the piezoelectric

coefficient d_{33} depends on the polarization per unit volume a large increase in the value of the piezoelectric coefficient is calculated. [Agrawal and Espinosa \(2011\)](#) reported an increase of e_{33} by a factor of 50 in 0.6 nm ZnO wires.

In Figure 3.6 we plot the change of thermal conductivity versus the strain induced by the electric field. The values of the electric field for each point are placed next to them. We can see that the decrease of the thermal conductivity follows almost the same trend as that for the mechanically strained case. This is direct evidence that the strain induced by the electric field is responsible for the modification of the thermal conductivity.

3.3 Thermal conductivity of bulk AlN crystals

3.3.1 Effect of system size on the thermal conductivity of aluminium nitride

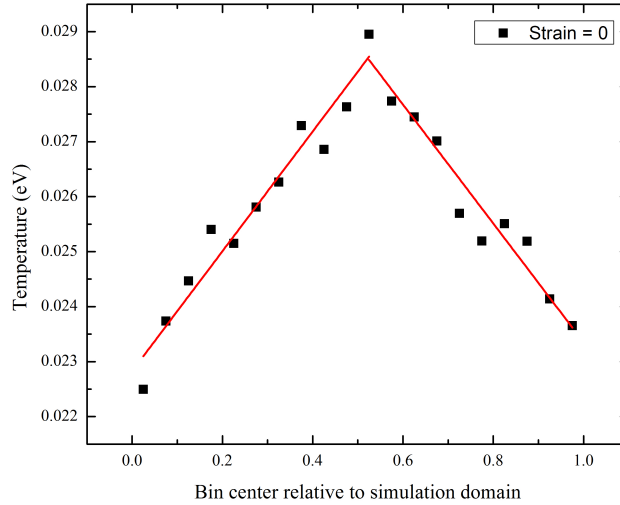


Figure 3.10: A representative graph of the temperature gradient of a $14 \times 8 \times 20$ AlN crystal at 300K during the data collection period. This is after 500 ps of applying the heat flux.

We have also performed the same study for AlN single crystals. The simulation domain size was $14 \times 8 \times 20$. The initial unit cell lengths were $a = 3.112$, $c = 4.982$ giving a domain of $37.73 \times 37.344 \times 99.64$ Å with 13440 atoms. The Vashishta ([Vashishta et al. \(2011\)](#)) potential was used with a cutoff of 7.6 Å. We used 80ps for initial equilibration followed by 500 ps to reach steady state, and 50ps for data collection. The heat exchange step size was $N_{mp} = 25$ which gave a temperature gradient of 1.2 ± 0.2 K/Å for the simulations. To study the size effect we performed two runs with

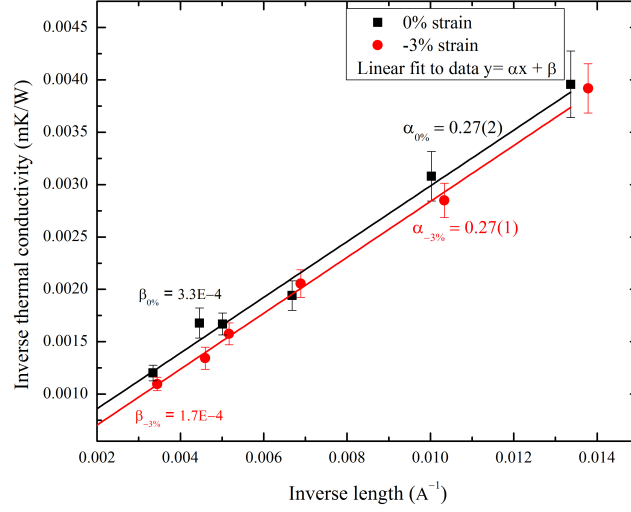


Figure 3.11: Effect of system length on the calculated thermal conductivity of AlN at 300K for 0 and -3% strain. The straight lines are the linear fit to the data with α as the slope and β representing the y-intercept.

system lengths of 15, 20, 30, 40, 45, and 60 unit cells in the Z-direction. The number of atoms was between 10080 and 40320, and the computation time was 40 minutes using 120 CPUs. In order to verify that the size effect is the same for different strain values, we repeated the calculations of thermal conductivity as a function of system length for a strained crystal. Following the initial equilibration period, the box length was scaled by a factor of 0.97 and then stabilized using NVT conditions. As we can see in Figure 3.11 the size effect is linear for 0 and -3% strain. At -3% strain we can see that the coefficient of proportionality between inverse length and inverse thermal conductivity is the same as that for no strain. This indicates that the strain does not affect the size dependence of the calculations for AlN. Hence, the same size adjustment can be made for all values of strain. Linear extrapolation of the values in Figure 3.11 provides the infinite length thermal conductivity at zero strain of 3000 W/mK. The thermal conductivity of a perfect AlN crystal at room temperature has been measured by Slack to be around 285 W/mK (Slack et al. (1987)). However, we should note that for the case of AlN there are always oxygen impurities and defects which reduce the thermal conductivity. In fact it oxygen acts as a substitutional impurity in AlN with concentrations up to $1 \times 10^{21} \text{ cm}^{-3}$ (Slack et al. (2002)).

3.3.2 Effect of uniaxial strain strain on the thermal conductivity of aluminium nitride

To study the effect of uniaxial strain on the thermal conductivity of AlN we have fixed the system length to 20 unit cells. The number of atoms was 13440. The Vashishta

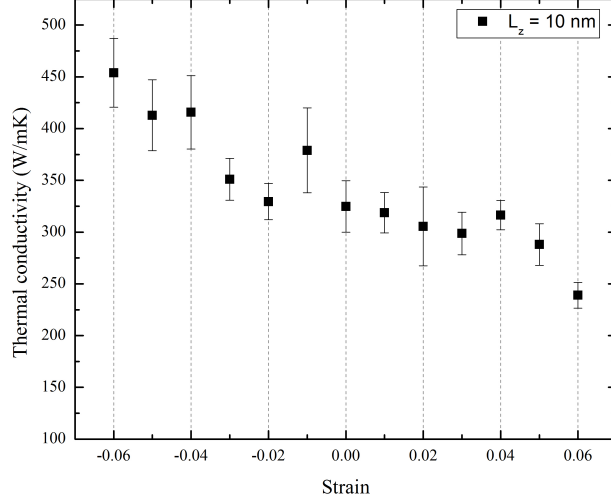


Figure 3.12: *Effect of strain on the calculated thermal conductivity of AlN at room temperature.*

potential was again used with the same cutoff of 7.6 \AA , and strain values from -0.06 to 0.06 in increments of 0.01 were used. The heat flux step size was kept the same $N_{mp} = 25$, and the temperature gradient was also the same at about 1.2 K/\AA . The strain was again applied simultaneously with the heat flux, and it was observed that after 500 ps the temperature gradient was acceptable to begin data collection. The effect of strain on thermal conductivity can be seen in Figure 3.12. First, we see that the effect of strain on the thermal conductivity of AlN is not the same as that seen in ZnO. One reason for this might be the different dominant bonding mechanisms in the two crystals. The effective charge in ZnO is $+2e$ and $-2e$ for zinc and oxygen ions, respectively. While in AlN it is $-1e$ and $+1e$. In addition, the interatomic potentials for ZnO, BKS and rigid ion models, have a larger ionic contribution. In fact, the potential requires the use of a long-range solver such as Ewald or Wolf summation. AlN, on the other hand, has been historically simulated using either Tersoff or Vashishta potential (Vashishta et al. (2011)) which do not contain long-range forces. Hence, the dependence of the phonon properties on the strain should be different. Especially for the optical phonon modes which are more affected by the strain as one can see in figure 3.8. We can see that the strong covalent nature of AlN inhibits any significant modification of the thermal conductivity for compressive and tensile strain.

Unfortunately, due to the strong large error associated with the calculation of the thermal conductivity of AlN we were not able to fit the size-corrected values to the same model $\kappa = a\epsilon^b$. The outlier values at -1% and <-4% strain values showed unphysical negative thermal conductivities when equation 3.11 was applied. It has been noted that for high-thermal conductivity crystals the NEMD is unsuitable (Termentzidis and Merabia (2012)).

3.4 Conclusions

1. We have studied the effect of strain on the intrinsic thermal conductivity on ZnO and AlN perfect crystals. We have noted that the strain effect is stronger in the case of ZnO than AlN. Seeing that the only difference between the two crystals is the inter-atomic bonding, we attribute the stronger dependence to the long-range forces (electrostatic) which are more present in the case of ZnO.
2. The change in the group velocities in ZnO is seen to mainly follow the trends of the thermal conductivity; however, the weaker drop when going from compressive to tensile strain suggests that modification of the relaxation times of the phonon modes must also be taking place. This is a reasonable assumption based on other studies, but one which was not verified.
3. Finally, we were able to verify the presence of a piezothermal resistive effect in ZnO. However, a real-life application cannot be confirmed as the values of the electric field to see a real change are above the dielectric breakdown limit.

Chapter 4

Thermal conductance - Kapitza resistance. Effect of local strain on thermal conductance of superlattices

In this chapter we study the effect of piezoelectric strain on the thermal conductivity of superlattices. We use equilibrium and non-equilibrium molecular dynamics to calculate the thermal conductance of SiO₂ and Si/Ge superlattices under various piezoelectric and mechanical strain strengths, respectively. We show that strain applied to the superlattice junctions induces large changes in the inter-layer conductance.

4.1 Literature review

When two different materials are placed in perfect contact, strain roughness, or defects between them will cause a finite thermal conductance at the interface when a heat flux is applied. The interface thermal conductance (ITC) is due to a combination of intrinsic and extrinsic sources, and may be defined in Eq. 4.1.

$$\sigma = q/\Delta T \tag{4.1}$$

Where ΔT is the temperature difference across the interface, and q is the thermal flux. In Kapitza (1941), experimental evidence of the presence of a thermal boundary resistance was shown for the case of liquid helium. This experiment showed that even for almost perfect contact there is always some resistance between two dissimilar materials. The discontinuity of phonon properties at the interface causes some back-scattering of phonons as they move across the interface. This resistance to the flux of phonons is what is called Kapitza resistance, and is an intrinsic property of the combined system. Other sources for phonon scattering at the interface may include scattering due to strain field or defects and voids. These are due to the manufacturing process, and are extrinsic effects.

For the intrinsic (Kapitza) resistance there are two limiting models for phonon transmission across an interface: the acoustic mismatch model (AMM) and the diffuse mismatch model (DMM). The AMM treats phonons as plane waves incident across the interface. The waves have a finite probability for reflection α_{AMM} which is due to the change in the acoustic impedance of the materials $z_i = \rho_i c_i$ where ρ_i is the mass density and c_i is the sound velocity. By applying the laws of classical acoustics the transmission probability for a longitudinal wave incident on the interface is given by equation 4.2 [Srivastava \(1990\)](#)[p.368]

$$\alpha_{AMM} = \frac{4z_1 z_2}{z_1 + z_2} \quad (4.2)$$

And the Kapitza conductance can be obtained by applying Debye's isotropic continuum model which assumes that: (1) only long-wavelength phonon modes are present in the whole \mathbf{q} -space $\omega(\mathbf{q}s) = c_s \mathbf{q}$, and (2) an average phonon-mode group velocity $\frac{3}{c^3} = \sum_s \frac{1}{c_s^3}$ where c_s is the phase velocity (transverse, longitudinal) and in this case is equal to the group velocity $c_g = c_s$ ([Srivastava \(1990\)](#)[p.48-49]). The expression for σ_{AMM} is given in equation 4.3

$$\sigma_K^{-1} = \pi^2 k_B^4 \alpha_{AMM} / 30 \hbar^3 c^2 \quad (4.3)$$

The result may be considered valid only for the long-wavelength phonons at low temperatures where the Debye approximation and wave-picture of phonons is dominant. The model also assumes that the interface is completely specular, and that no scattering takes place.

The diffuse mismatch model, on the other hand, assumes that the phonons are completely diffusely scattered at the interface. In other words, the phonons lose their history when they reach the interface. The transmission coefficient in this case is determined by the overlap between the densities of states between the two materials. The expression for the phonon transmission under the DMM can be found from the principle of detailed balance. The two models represent the two extremes of phonon behaviour at an interface. For example, at high acoustic dissimilarity $z_1/z_2 \neq 1$ the DMM is predicted to reduce the thermal boundary resistance calculated from the AMM. While at low mismatch, diffuse scattering increases the thermal boundary resistance; more precisely, it is doubled compared to the acoustic model. In fact, for the limit $z_1/z_2 \rightarrow 1$ the DMM gives the unphysical conductance related to $t_{DMM} = 0.5$, where t is the transmission probability across the interface, while the AMM gives the more physically sound value of unity. The DMM is noted to be valid for high frequency or short-wavelength phonons at high temperatures.

For solid-solid interfaces which do not suffer from large acoustic dissimilarity, the values for the Kapitza resistances predicted from the two models are relatively close (a difference of about 30% [Srivastava \(1990\)](#)[p.369]). Hence, experimental results usually agree well with both models. To improve the agreement an interpolation between the two models can be implemented as was done in [Kazan \(2011\)](#). The model in [Kazan \(2011\)](#) utilized the RMS roughness of the interface in comparison with the phonon-mode wavelength to determine whether phonons would be scattered diffusively or specularly. The model also takes into account the full bulk dispersion relations for the two sides for the calculation of the group velocity of phonon-modes,

and for calculating the density of states. The model showed very good agreement with experimental results for InN/GaN interfaces.

Another important consideration when predicting the Kapitza resistance is the interfacial strain due to the lattice mismatch between the two sides of the interface. The difference in lattice constants creates dislocations at the interface as the atoms are displaced from their equilibrium position (i.e. with no interface). The displacement creates a space dependent strain field which relaxes as one goes further into the bulk of either side of the interface. However, the finite modification of the atom positions just at the interface leads to a change in the elastic coefficients, and this change can be shown to depend on the third-order force constants. The spatial dependence of the elastic coefficients can be shown to scatter phonons, as was shown in Carruthers (1959), and that a characteristic relaxation time τ_{strain} can be defined. In Meng et al. (2013) this analysis was carried out. Two dissimilar lattices were considered as seen in Figure 4.1. In this figure the interface strain field (ISF) determining the displacement of atoms is periodic in x (parallel to the interface), and is exponentially decreasing in z (normal to the interface) which makes it a short-range field. The larger is the dissimilarity between the two lattices, the shorter is the range of the strain field in the normal direction to the interface. (Meng et al. (2013)) It was shown in Meng et al.

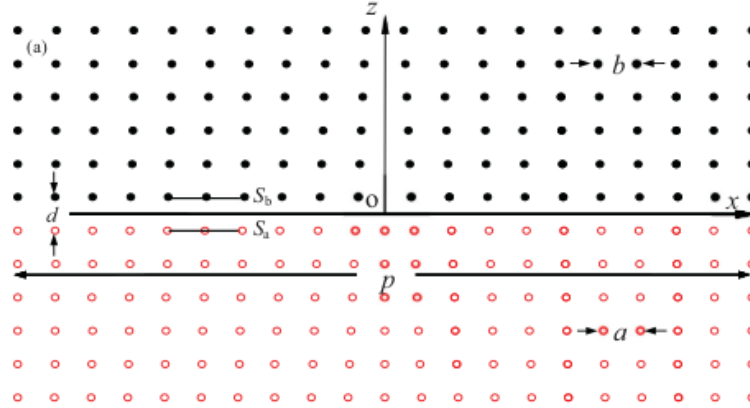


Figure 4.1: A schematic showing the dislocation due to mismatched lattices. The black dots and red circles represent the atom positions on the two lattices. S_b , S_a are the contact planes, and p is the distance between dislocations. It also represents the dissimilarity between the two lattices. Smaller p indicates more dissimilarity. From Meng et al. (2013)

(2013) that the interface strain field scatters phonons above a critical frequency ω_0 which depends on the amount of dissimilarity between the two lattices p . Hence, a gradual switch from a DMM dominated to an AMM dominated phonon-transmission scheme is obtained as the dissimilarity between the lattices increases (Meng et al. (2013)). The work also showed that the scattering time is different than that seen in a single bulk dislocation. The inverse scattering time for an interface strain field (ISF) is $1/\tau_{ISF}(\omega) \propto (\omega - \omega_0)^3$ whereas for an individual dislocation it is given by the relation $1/\tau(\omega) \propto \omega$ (Meng et al. (2013)). And finally, by using the Callaway model for the thermal conductivity, it was shown that the effect of the ISF is to decrease the thermal conductivity relative to the a system with no ISF scattering at high temperatures. Nevertheless, this change is relatively small in solids, approximately 10% of

the DMM at 300K, and as such it does not dominate the interface conductance (Meng et al. (2013)).

Meng et al. (2013) nevertheless showed that the effect of in-plane strain does have an effect on the cross-plane thermal conductance. This effect is in essence due to the anharmonicity of the inter-atomic potential across the interface. Therefore, and as pointed out in Shen et al. (2011) neither the AMM nor DMM account for the stiffness of the interface. The stiffness is defined as the change in the normal to interface stress to the normal strain $S = \partial P_{zz} / \partial \varepsilon_{zz}$. The value of S determines the strength of the bonding, and is related to the inter-atomic potential. For a harmonic potential it is constant, but for an anharmonic potential it depends on the separation between the two solids. In Shen et al. (2011) the thermal conductance between two Lennard-Jones type solids was calculated using NEMD simulations for different bonding strengths. It was shown that for weak interfaces (the interfacial bonding is weaker than the bulk bonding) the application of uniaxial pressure normal to the interface increases the thermal conductance while for strong interfaces there is no change in the conductance, rather there is a slight decrease for large pressure values. The increase in conductance was shown to be correlated with the increase in interface stiffness S while the increase in the bulk stiffness (or modulus) is seen to decrease the interface conductance. In weak interfaces the former effect is dominant while for strong interfaces, the two effects cancel out. The decrease of the conductance due to the increase in bulk modulus is due to a change in the phonon transmission coefficients. For even though the increase in the bulk modulus means an *increase* in the group velocities and frequencies of the modes, the results indicate that the thermal conductance *decreases*. It was postulated that this is due to a decrease in the phonon transmission probabilities. In the harmonic approximation, the overlap between the densities of states from each side is what determines the transmission probabilities (DMM), and it was shown in Shen et al. (2011) that the conductance between two mass-dissimilar solids does indeed follow this overlap. The harmonic contribution to the thermal conductance was also shown to be dominant in Sääskilähti et al. (2014). In said article, MD simulations were used to calculate the thermal conductance of two fcc LJ solids. A frequency resolved expression for the elastic and inelastic thermal conductances were developed, and it was shown that pressure does not affect the transmission of energy for low frequency modes by elastic forces nor for inelastic transmission. Hence, it is elastic processes for high-frequency modes that affect the thermal conductance under uniaxial compression. The observed increase due to compression was roughly 26% for 42 MPa. In complex crystals the density of these high frequency modes can be rather significant, and it might be possible to affect the thermal conductance even more.

An example of such a weakly-bonded system is silica-graphene superlattices. Silica is regularly chosen for graphene deposition due to the low mismatch between the lattices. In Hsieh et al. (2011) experimental determination of the dependence of thermal conductance of Al/graphene/SiO/SiC films on the uniaxial pressure was measured using time-domain thermoreflectance. From normal up to 10 GPa, it was noted that the thermal conductance of such a structure is strongly dependent on the pressure. An increase of about a factor of 5 is seen for low pressure (up to 6 GPa). However, it was noted in that work that the dependence of the conductance on pressure for clean Al/SiO/SiC was very similar to that of the system with graphene. A result which was surprising, and may have cast doubt about the contribution of graphene to the results.

Nevertheless, the effect of pressure on such weak interfaces was verified experimentally, and the thermal interface conductance of silica/graphene was determined to be around $25 \text{ MW.m}^{-2}.\text{K}^{-1}$ at normal pressure. The pressure dependence was also verified using molecular dynamics by the same group of [Shen et al. \(2013\)](#) and by the group of [Mak et al. \(2010\)](#) experimentally using time-domain thermoreflectance. Both works have also noted that the number of graphene layers does not affect the thermal conductance albeit that the inclusion of more graphene would increase the total resistance of the system.

To recap, the DMM and AMM offer the two extremes of phonon transmission across interfaces at normal conditions. However, they donot take into account the strength of the bonds across the interface. The presence of a local strain field at the interface modifies the elastic properties of the system and leads to phonon scattering. The scattering depends on the phonon frequency, and ths strain field spatial extent. It has also been demonstrated both experimentally and using MD simulations that the application of pressure to weakly-bonded systems modifies their thermal conductance. Therefore, it is our aim in the next few sections to study the effect of local strain on the thermal conductance of such systems, and show that they are good candidates for piezothermal application.

4.2 Effect of non-uniform strain on the thermal conductance of SiGe superlattices

We begin by taking a simple system consisting of a $10 \times 10 \times 20$ SiGe superlattice shown in Figure 4.2. In the cross-plane direction we create 10 unit cells of germanium and 10 unit cells of silicon. The number of atoms is 16000. The conventional diamond unit cell was used for both lattices. The Tersoff ([Tersoff \(1989\)](#)) potential was used for both elements, as mixing rules exist for Si and Ge. Simulations of each material, separately, gave unit cell lengths for germanium and silicon corresponding to $a_{Ge} = 5.6711\text{\AA}$, $a_{Si} = 5.4423\text{\AA}$. To build the superlattice, the mean unit cell length was used $a_{Ge/Si} = (a_{Ge} + a_{Si})/2 = 5.5567\text{\AA}$ as starting guess for both structures. This strains the original unit cells of Ge and Si by -2% and 2.1%, respectively. In order to study the effect of in-plane and cross-plane stress three types of simulations were carried out. (1) A simulation where the initial structure was relaxed *only* in the Z direction, (2) another where the initial structure was relaxed in *all* three directions, (3) and a final where the structure was relaxed in all three directions however later a *non-uniform* strain was applied in the Z direction. The superlattice thermal conductance for all simulation types was calculated using the reverse NEMD algorithm where a heat flux was simulated in the system by exchanging particle velocities and a corresponding temperature drop can be observed across the interface; exactly the same algorithm used in the previous section. For the third type of simulations (non-uniform strain) two strain values were investigated: $\pm 1\%$ and $\pm 2\%$. For all simulations types only one run was performed with the following general scheme:

1. *Relax structure - 100 ps*

The timestep is set to 1 fs, and periodic boundary conditions are applied along

all sides. The structure was relaxed in the designated directions (Z -only or X Y , and Z under 0 GPa and 300K (NPT ensemble).

2. *Strain and apply heat flux*

Any required strain is applied to the structure by remapping the coordinates of some of the atoms, and the heat flux is applied to the strained system. The velocity swap is performed every 20 fs (20 timesteps).

3. *Reach steady-state - 500ps*

The system is allowed to reach steady state under NVT conditions. The temperature profile is monitored, and 500ps were sufficient to obtain a reasonable flat temperature profile away from the interfaces.

4. *Collect data - 50ps*

After steady state has been reached, we collect the temperature profile, in-plane and cross-plane pressure, and the energy exchanged from the velocity exchange.

5. *Data analysis*

The average temperature profile ΔT , area A , system length L_z , and heat flux q are then used to calculate the thermal conductance using equation 4.1.

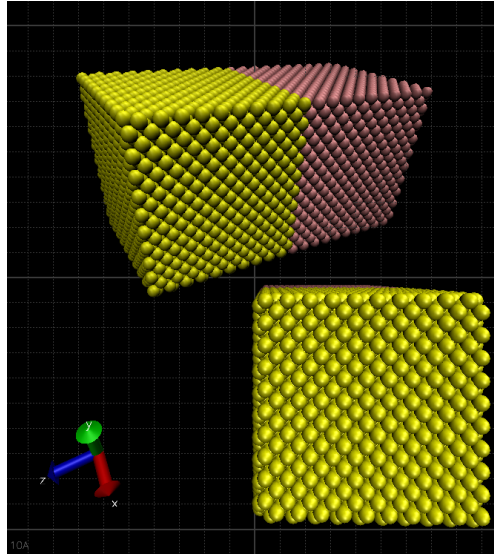


Figure 4.2: *Perspective and in-plane view of SiGe superlattice $10 \times 10 \times 20$ before start of simulation. Ge atoms are in yellow and Si atoms are in pink.*

Procedure for creating a non-uniform initial periodic strain state In order to apply a non-uniform strain to the superlattice, the following procedure was adopted. After equilibrating the superlattice under NPT, a central group of atoms was selected. This central region has a length of 3 unit cells. The simulation box was then rescaled in the Z direction, and the corresponding central atoms remapped according to the rescaling. This creates a non-uniform periodic strain in the superlattice, and forces the atoms to adopt new equilibrium positions. A schematic of this procedure (tensile

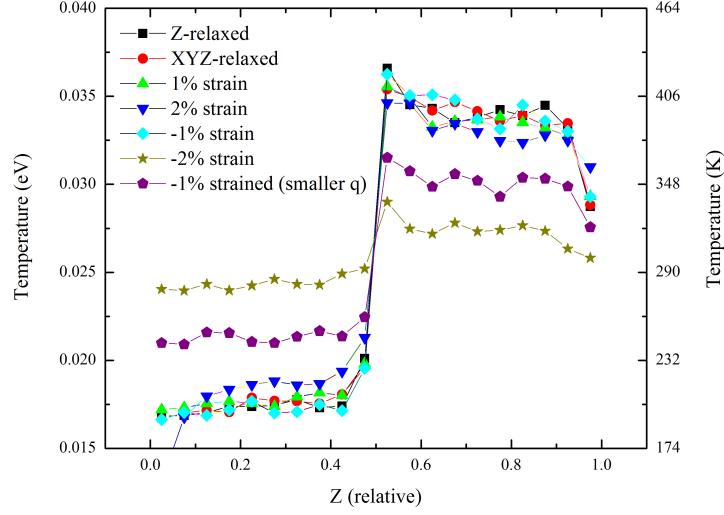


Figure 4.3: Temperature profiles for the different simulation types of the SiGe superlattice. The profiles shown are collected at the end of the simulation.

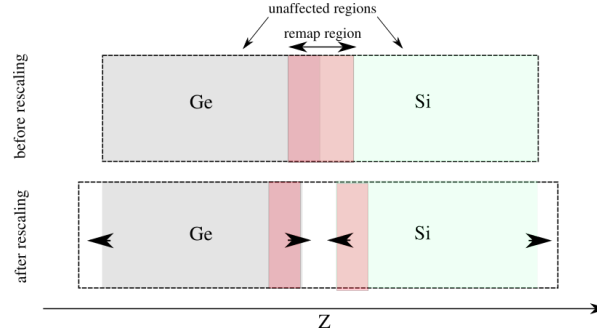


Figure 4.4: A schematic showing the rescaling of the simulation box for the case of tensile strain. The figure is to scale in the Z-direction; however, the rescaling is exaggerated for clarity. The operation is performed after the equilibration period, and the superlattice is allowed to relax under NVT conditions. The arrows represent the restoring forces arising from the remapping of the atoms.

strain) is shown in Figure 4.4. As can be seen in the figure, the operation creates an initial state of non-uniform strain.

The temperature profile was sampled away from both interfaces (periodic boundary conditions). Sample temperature profiles for all simulation types are shown in Figure 4.3. 500 ps were sufficient to obtain an almost constant heat-flux q and temperature profile for all simulation types except the -2% strained superlattice which showed a non-linear temperature profile. Hence, the heat flux was decreased. The results for all simulations are presented in Table 4.1.

System type	q ($\times 10^9$ W/m ²)	ΔT (eV)	σ ($\times 10^9$ W/m ² K)	P_z (GPa)
Z-relaxed	28.86 ± 0.7	0.0167 ± 0.0003	0.074 ± 0.003	0.0889
XYZ-relaxed	796 ± 20	0.0165 ± 0.0004	2.07 ± 0.1	-0.154
1%-strain	29.1 ± 0.7	0.01589 ± 0.001	0.078 ± 0.007	-1.31
2%-strain	23.6 ± 0.7	0.01418 ± 0.001	0.072 ± 0.007	0
-1%-strain	28.4 ± 0.8	0.01693 ± 0.0008	0.0723 ± 0.0053	1.31
-2%-strain	16.59 ± 0.6	0.00323 ± 0.0009	0.2215 ± 0.07	2.20
-1%-strain	14.5 ± 0.6	0.00889 ± 0.0007	0.0704 ± 0.008	1.31

Table 4.1: Thermal conductance results for the various simulation types of SiGe superlattices. The errors are the standard deviations of the averages during the data collection period. P_z is the average pressure at the end of the simulation.

For the fully relaxed case, we obtain a thermal conductance $\sigma_{Si/Ge}$ of 2.07 GW/m²K which is reasonable when compared to the value of 0.34 GW/m²K at 500K reported in other works (Chalopin et al. (2012), Landry and McGaughey (2010)). However, as the results in Table 4.1 show, there is a significant drop in the thermal conductance when comparing the fully relaxed superlattice to all the other types (a factor of 28 reduction). For the Z-relaxed superlattice, the final cross-plane stress, P_z , is more than a factor of 10 lower than for the $\pm 1\%$ or -2% strained case (for the 2% case we theorize that the atoms were displaced a distance larger than the cut-off for the potential thereby giving the lowest stress value). This confirms that the two cases Z-relaxed and initially-strained do not share the same final state in terms of residual cross-plane stress. Nevertheless, we remark that the thermal conductance is almost the same (0.074 GW/m²K). This suggests that in-plane stress is just as effective as cross-plane stress in affecting the thermal conductance. The -2% strain case also shows that the thermal conductance goes through a minimum under compressive strain. To verify that the higher conductance value ($\sigma_{-2\%} = 0.22$ GW/m²K) is not due to numerical artefacts, we performed an extra simulation (-1%) for a lower value of q . We obtain the same value of thermal conductance which indicates that the calculation of the thermal conductance is insensitive to the value of the applied heat flux.

4.3 Molecular Dynamics simulation of the thermal conductance of SiO₂/FLG superlattices

We have also calculated the thermal conductivity of silica/graphene interfaces using EMD simulations. The calculation of the thermal conductance of silicon/graphene superlattices (σ_{SiOC}) has been performed in a recent work using NEMD (Shen et al. (2013)), and it has been determined that the number of graphene layers does not affect the thermal conductance. Using experiments, as well, (Mak et al. (2010)), it has been determined that the number of layers from 1 to 13 does not affect the conductance between silica and graphene. Hence, we have simulated a 4×6 superlattice of silica/graphene with 7 unit cells of silica, and 3 monolayers of graphene. A snapshot of the superlattice is shown in Figure 4.5 after initialization of the atom coordinates. Silica quartz (SiO₂) belongs to the trigonal P3₂21 space group. It has

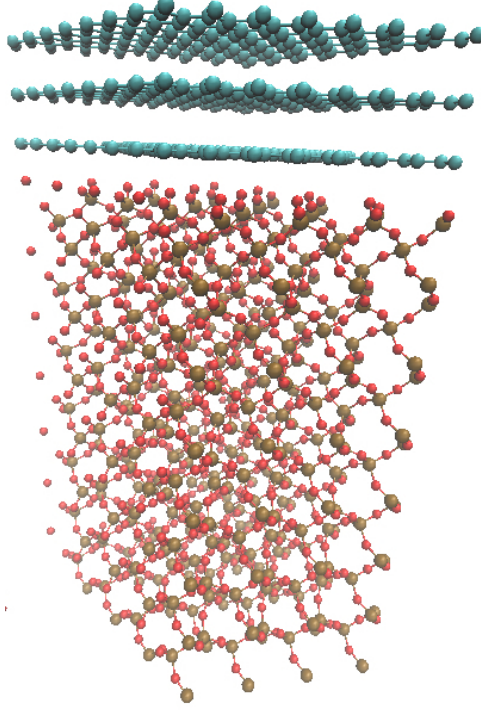


Figure 4.5: A snapshot of silica/graphene superlattice used for all simulations with 3 monolayers of graphene (green atoms) and 7 unit cells of silica or α -quartz. The electric field is applied in the cross-plane direction.

lattice constants given by $a = 4.97636\text{\AA}$ and $c = 5.4397\text{\AA}$, and the unit cell contains 9 atoms. Graphene belongs to the $P6_3/mmc$ space group with lattice constants given by $a = 2.4569\text{\AA}$ and inter-sheet spacing $0.5c$ where $c = 6.708\text{\AA}$ (from graphite structure). The two-dimensional unit cells contains 2 atoms. The cross-sectional area of the superlattice is approximately $342 \pm 5\text{\AA}^2$ while the initial length is approximately 56.74\AA . The number of atoms is 2844 atoms. The BKS potential (van Beest et al. (1990)) with a cutoff of 5.5\AA was used to simulate the interaction between silicon and oxygen atoms. Wolf summation with a cutoff of 10\AA and a damping parameter $\alpha = 0.3$ was used to calculate the electrostatic interactions. The charges on the silicon and oxygen atoms are $+2.4$ and -1.2 , respectively. For the carbon atoms the AIREBO potential (Stuart et al. (2000)) with a cutoff of 3.0\AA was used. To simulate the interactions between the graphene layers and silica atoms the Lennard-Jones potential was used with parameters taken from Ong and Pop (2010). The LJ interactions are suitable for the modelling of physisorbed graphene on silica substrates, and they model the weak bonding forces of such superlattices. The equilibrium separation between O face of the silica and the graphene by minimizing the potential energy of the total system was found to be $d_{O/C} = 3.3622\text{\AA}$ while that for Si was $d_{Si/C} = 3.6758\text{\AA}$. The equilibrium distances $r_m = 1.122\sigma$ obtained from the LJ parameter σ are $r_m = 3.367\text{\AA}$ for O-C and $r_m = 3.732\text{\AA}$ for Si-C which correspond well to the values obtained by minimization. Periodic boundary conditions were applied in all three directions, and the timestep was set to 1fs.

In order to calculate the thermal conductance, we used the equilibrium method of temperature fluctuations (Rajabpour and Volz (2010)). The inter-layer resistance $R_{SiO/C}$ is given by equation 4.4

$$Rk_B = \int_0^\infty \frac{\langle \Delta T(0) \Delta T(t) \rangle}{\langle \Delta T(0)^2 \rangle} dt \left(\frac{1}{N_1} + \frac{1}{N_2} \right) A \quad (4.4)$$

Where the subscripts 1,2 represent the two thermal reservoirs, in this case the silica and graphene, ΔT is the temperature difference between the interacting atoms of the two reservoirs, A is the surface area, and $N_{1,2}$ is the number of potential and kinetic degrees of freedom on a given side which is related to the number of atoms. The thermal conductance was calculated as a function of electric field.

After initialization of atom positions, momenta, and forces, the system was equilibrated under NPT conditions while applying a static electric field in the Z direction for 300 ps. The temperature difference between carbon and silica atoms was then sampled for 800 ps under NVT conditions. The interacting atoms were selected by specifying rectangular regions close to the first and third graphene layers. The height of this region was set to 4.2\AA to try and include only first interacting layers of atoms. The number of silica atoms was found to be $N_1 = 227$ and that of graphene to be $N_2 = 180$. 10 independent simulations were performed for each value of the electric field.

Quartz is a well known piezoelectric crystal. It belongs to point group 32. The piezoelectric tensor is given by equation 4.5 in Voigt notation. The tensor determines the magnitude of the converse piezoelectric effect $\epsilon_i = d_{ij}E_j$.

$$d_{ij} = \begin{pmatrix} d_{11} & -d_{11} & 0 & d_{14} & 0 & 0 \\ 0 & 0 & 0 & 0 & -d_{14} & -2d_{11} \\ 0 & 0 & 0 & 0 & 0 & 0 \end{pmatrix} \quad (4.5)$$

The application of a static electric field parallel to the c -axis of SiO_2 crystal produces

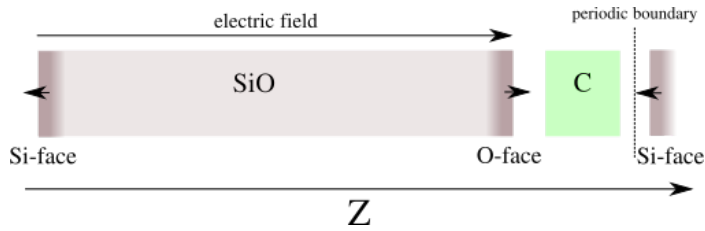
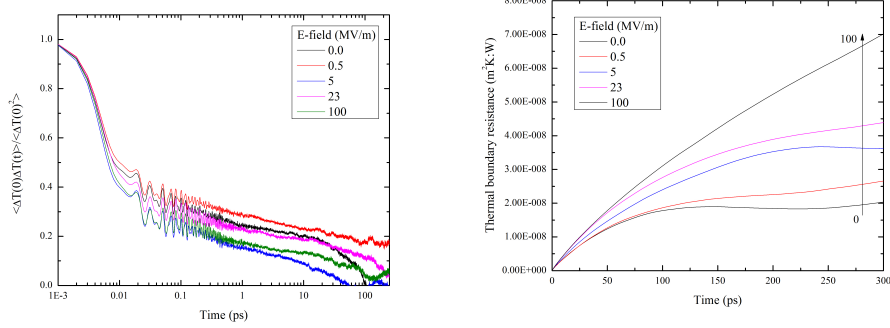


Figure 4.6: Schematic representation of the SiOC superlattice with the application of an electric field leading to local compressive strain at the interfaces. The arrows represent the electrostatic forces at the end surfaces. Figure not to scale.

no bulk strain $d_{i3} = 0$. Nevertheless, in the SiO_2/C superlattice the end surfaces of the SiO_2 lattice will still experience strain because of end effects. The application of a positive electric field will lead to local compressive strain at the superlattice junction as represented in Figure 4.6. This should lead to a situation similar to that seen in the Si/Ge superlattice, and to a reduction of the thermal conductance. In Figure 4.7, we plot the cumulative integral of the autocorrelation function. From that we



(a) Example of the autocorrelation of temperature difference in one simulation between the interacting graphene and silica atoms. (b) Average of the cumulative integral of the autocorrelation function giving the accumulation of the thermal boundary resistance. 10 simulations for each graph.

Figure 4.7: The thermal boundary resistance as a function of simulation time for several electric field strengths in MV/m.

obtain the thermal resistance. We can see that for zero electric field the thermal conductance is well converged to its final value within 300 ps. The final resistance at zero electric field is $1.85 \pm 0.15 \times 10^{-8} \text{ m}^2\text{K/W}$ which gives a thermal conductance $\sigma_{\text{SiO/C}} = 1/R = 5400 \pm 440 \text{ W/cm}^2\text{K}$. The value is in very good agreement with experimental findings (Mak et al. (2010)). For 0.5 MV/m, we can see an increase in the resistance by a factor of 1.2. This value is determined at $t = 200 \text{ ps}$. For later times the resistance is seen to diverge slightly due to insufficient averaging. For higher values of the electric field, 23 MV/m, the thermal resistance continues to increase by a factor of 2, and does not seem to attain its final value within 300 ps. The short time behaviour of the thermal conductance is also seen to change most significantly at 5 MV/m. The temperature autocorrelation function is often given as in equation 4.6 to indicate the two predominant mode relaxation times (Rajabpour and Volz (2010))

$$\frac{\langle \Delta T(t) \Delta T(0) \rangle}{\langle \Delta T(0)^2 \rangle} = A_{\text{short}} e^{-t/\tau_{\text{sh}}} + A_{\text{Long}} e^{-t/\tau_{\text{Lo}}} \quad (4.6)$$

The change in the short time behaviour ($< 50 \text{ ps}$) of the thermal resistance indicates that at high electric field values the induced local strain field begins to affect the short-lifetime modes. Unfortunately, we were not able to accurately calculate the inter-layer strain. An estimation of it should show an increase in the spatial extent and magnitude. The results of such an increase would be in agreement with theoretical models which indicate a relationship between the properties of the interfacial strain field and the frequency of phonon modes affected by it.

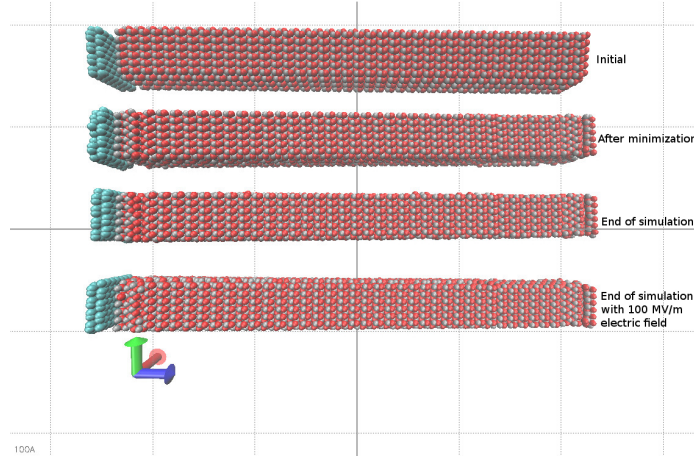


Figure 4.8: Snapshots of ZnO/C superlattice at different stages of the simulation with and without an external electric field. Carbon atoms are in green, and are placed on the Zn face. Note the reconstruction of the ZnO lattice at the free ends.

4.4 Molecular dynamics simulations of ZnO/FLG superlattices

We have also studied the effect of electric field on the thermal conductance of ZnO/C superlattices. We have simulated $7 \times 4 \times 40$ ZnO lattice with 2 monolayers of graphene placed at the Zn face as seen in Figure 4.8. The graphene atoms were strained to the ZnO lattice in the in-plane direction. This induces a strain of -14%. For ZnO we used the same potential as before (PCRM), for carbon we used the AIREBO potential, and for the Zn-C and O-C interactions, the Lennard-Jones potential. The interaction between ZnO and graphene has been studied, and MD simulations have demonstrated that Lennard-Jones interactions reproduces real physisorbed graphene on ZnO substrates very well (Galan and Sodano (2012)). Hence, we use parameters for Zn-C and O-C interactions taken from Guo et al. (2011) and Harris and Yung (1995), respectively. Stabilization of the ZnO structure is an important issue as well. Electrostatic interactions in ZnO are dominant, and the morphologies of the (1000) and (0001) surfaces are dependent on their respective polarities. In order to stabilize ZnO nanowires, for example, which expose the polar surfaces, three methods are available:

1. Surface passivation by the saturation of surface bonds using (OH^- or H^+ molecules) (Lauritsen et al. (2011)).
2. Reconstruction of the polar surfaces into a shell like structure by the relaxation of the outermost ions (Jedrecy et al. (2000), Kulkarni and Zhou (2006)).
3. Reduction of the charge on the Zn-surface by charge transfer of some O^- ions from the O-surface. This results in the reduction of the surface charges by 0.75S (Dai et al. (2011), Noguera (2000))

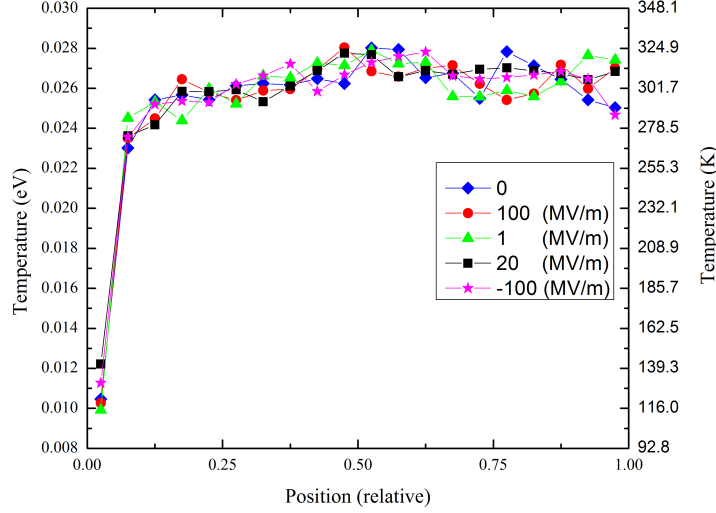


Figure 4.9: Temperature profiles of ZnO/C superlattices at the end of the simulations for different electric field strengths. The first point corresponds to the temperature of the double monolayers of graphene (cold slab).

All the stabilization methods are confirmed to affect the thermal conductivity of ZnO nanowires due to the modification of surface phonon modes (Jiang et al. (2013)). In our case of ZnO/C superlattices, the addition of the graphene layers in between the ZnO layers seems to keep the ZnO system stable. This is accompanied by some reconstruction of the end (polar) surfaces as can be seen in Figure 4.8. Nevertheless, the structures were stable until the end of the MD simulations.

In order to calculate the thermal conductance, we again use the reverse NEMD method employed in section 4.2. We first minimize the total energy of the structure using the conjugate gradient method. The equilibrium separation between the end ZnO faces and the graphene is seen to deviate from the equilibrium distances initially applied and deduced from the Lennard-Jones characteristic distances by the formula $d_{eq} = 1.122\sigma$. We equilibrate the system under NPT conditions for 100ps. Then, we apply the electric field along the Z-direction as well as the heat flux, and we allow the system to reach steady-state under NPT conditions for 800ps. The temperature profile, heat flux, and system length are then sampled every 1.5ps for 50ps. It was not possible to obtain an accurate estimation of the strain induced in the system due to the electric field, as the addition of the graphene layers causes fluctuations in the system size on the order of the strains induced. The velocity of the atoms in the hot (ZnO) and cold (C) slabs are exchanged every 0.15ps leading to an average temperature difference of about 190K between the ZnO and graphene layers. The temperature profile of the ZnO is seen to be almost constant as shown for all values of electric field in Figure 4.9. The thermal conductance is calculated according to equation 4.1, and the results are given in Table 4.2.

E-field (MV/m)	q GW/m ²	ΔT eV	σ_{ZnOC} GW/m ² K
0	31.25 \pm 4	0.01603 \pm 0.0009	0.168 \pm 0.03
100	30.36 \pm 4	0.01606 \pm 0.0009	0.163 \pm 0.03
1	30.41 \pm 4	0.01632 \pm 0.0010	0.161 \pm 0.03
20	30.49 \pm 5	0.01425 \pm 0.0009	0.184 \pm 0.04
-100	30.51 \pm 3	0.01514 \pm 0.0009	0.174 \pm 0.02

Table 4.2: Thermal boundary resistance of ZnO/C as a function of electric field strength.

Not very surprisingly, it is found that the thermal conductance of ZnO/C is not affected by the application of the external electric field. The results in Table 4.2 show that the conductance is constant at a value of 170 MW/m²K for field strengths between -100 and 100 MV/m. ZnO is a piezoelectric crystal much like SiO₂. Unlike SiO₂, however, ZnO does possess a piezoelectric constant d_{33} leading to uniform strain when an external electric field is applied. This uniform strain is seen to not affect the thermal conductance between ZnO and graphene. The uniform extension and compression of the ZnO lattice merely displaces the graphene layers without any local deformation. This implies that the reconstructed polar surfaces are also unaffected by these values of the electric field.

4.5 Conclusions

Through several molecular dynamics simulations of different superlattices, we have seen that the interfacial thermal conductance is affected by the application of local strain at the interface. The interfacial conductance is observed to be highly sensitive to local strain for the case of perfect interfaces. The conductance is seen to be sensitive to residual strain in unrelaxed structures. For relaxed structures (those corresponding to real-life situations) the conductance is not affected by the application of additional compressive or tensile strain as seen in the case of SiGe ($\pm 1\%$ strain). However, for larger compressive strain values perpendicular to the interface, an enhancement of the conductance is possible. The effect has been explored in other MD simulations, and in experiments on silica/graphene interfaces.

The reduction of the conductance in silica/graphene superlattices has been shown to be effective for electric field strengths of 5 to 20 MV/m. This reduction is attributed to the particularity of the piezoelectric nature of SiO₂ which prohibits any bulk uniform strain while allowing for the creation of very local junction strain/stress. Unfortunately, we were unable to quantify this stress, and it remains to be calculated as confirmation to the proposed strain picture. For electric field higher than 25 MV/m we were unable to calculate the thermal resistance due insufficient simulation time. No decrease in the thermal resistance was observed for compressive strains as seen in other works (Shen et al. (2013), Shen et al. (2011)). The zero-field value of the thermal conductance of silica/graphene was noted to be in very good agreement with experiment (Mak et al. (2010)).

Finally, using ZnO/C superlattices, we were able to show that the thermal conductance is only affected by local strain. The application of a uniform static electric field to ZnO/C superlattice is predicted to induce a uniform strain field compared to the local strain field in the case of SiO₂/C. Reverse NEMD simulations indicate that the thermal conductance of ZnO/C superlattices is 170(5) MW/m²K.

Chapter 5

Conclusions and future work

5.1 Conclusions

With a combination of equilibrium and non-equilibrium molecular dynamics simulations we have studied the effect of strain on the thermal conductivity of bulk piezoelectric crystals and on the thermal conductance of piezoelectric superlattices. We have investigated the effect of uniform and non-uniform strain applied mechanically or using an electric field in piezoelectric crystals. The main conclusions of the work are as follows:

The thermal conductivity of bulk piezoelectric crystals ZnO and AlN have been calculated using reverse-NEMD. The zero strain values deviate greatly from experimental values. However, for the case of ZnO they have the same order of magnitude. It is seen that the effect of system size plays a significant role on the calculation of the thermal conductivity using reverse-NEMD, but that it follows the equations present in literature. Uniform uniaxial mechanical strain is seen to decrease the thermal conductivity going from compression to tensile. The behaviour of the thermal conductivity is that predicted for argon-like crystals and has the form $\kappa \propto \varepsilon^b$ where $\varepsilon = l/l_0$ and $b = -18.8$ for ZnO. The change in thermal conductivity in bulk crystals has been indicated to result from the change in the properties of the phonon modes i.e. the frequency, group velocity, and scattering rates. The dependence of thermal conductivity on strain is seen to depend on the size of the system with bigger systems showing larger coefficients of proportionality as the size effect becomes less dominant. It was also confirmed that strain induced using an external uniform electric field affects the thermal conductivity in the same way as that for strain induced mechanically. The phenomenon may be termed thermo-piezoelectric. However, the strengths of such fields exceed typical dielectric-breakdown values, and are therefore unattainable. By performing the same study on AlN we have shown that the dependence of thermal conductivity on strain is dependent on the type of atomic interactions. The more covalent nature of AlN which is a material with a higher Debye temperature suppresses the dependence of thermal conductivity on strain. Therefore, the thermal conductivity of ZnO is seen to have a stronger dependence on strain than that of AlN, and may be considered as a better candidate for piezothermal applications.

We have also investigated the effect of strain on the thermal conductance of superlattices of SiGe, SiO₂/C, and ZnO/C. We have shown that for SiGe superlattices the thermal conductance can decrease by a factor of 28 due to in-plane and cross-plane stress applied at the interface. We have shown that by initially straining the atoms at the superlattice junctions compressively and tensile we are able to create a final state where the thermal conductance is reduced as compared to an unmodified structure. The conductance is seen to reach its final value for 1% strain, and that larger initial tensile strains do not lead to further reduction in the conductance. Furthermore, larger initial compressive strains are seen to reasonable enhancement of the conductance in accordance with studies seen in literature which studied the case of constant uniform external pressure.

We have also examined two different cases of piezoelectric crystals: SiO₂/C and ZnO/C. The strain-free thermal conductances were calculated as 0.05 and 0.167 GW/m²K, respectively. It was shown that only in the case of SiO₂, a modification of the thermal conductance is possible, and that for a value of 20 MV/m of the electric field, it is possible to reduce the conductance by half. While for ZnO/C superlattices, the uniform strain induced by the piezoelectric phenomenon does not affect the thermal conductance.

The possible applications of such findings in piezo-thermal devices could be envisioned. For the case of superlattices, it is seen that the modification of the thermal properties is more pronounced than that for bulk materials. However, the systems presented in this work represent perfect interfaces. A situation that requires careful fabrication techniques. The case of SiO₂/C seems the most promising as the dielectric breakdown field of SiO₂ is in the range of 10 MV/m (Lynch (1972)) depending on the thickness.

5.2 Future works, perspective, and issues

The study presented in this thesis has attempted to explore various avenues for strain-modification of thermal conduction by phonons. As such it has attempted to explore different materials and interesting combinations. However, the mechanisms behind the situations where the thermal conductivity/conductance was modified were not fully explained. Therefore, there remains a lot to understand in these particular systems.

For the case of bulk crystals, the discrepancy between the AlN and ZnO results requires a more careful determination of phonon properties. The mode-specific relaxation times and group velocities need to be calculated in order to see why strain is effective in modifying the thermal conductivity of bulk ZnO crystals but not AlN. Arguably, such analysis has been performed, and is seen that the contribution of the different mode properties may not be intuitive. For high-Debye temperature crystals like AlN the contribution of the change of the heat capacity must also be considered as it was shown to change as a function of the strain (Parrish et al. (2014)).

For the case of the change in thermal conductance in superlattices. The most pressing issue is to quantify the local strain fields induced due to the initial straining of the atoms for the case of Si/Ge superlattice, and due to the electric field in the case of

SiO₂/C superlattices. It is important to quantify the spatial extent and magnitude of the strain fields, and to see whether they correspond with theoretical models developed elsewhere ([Meng et al. \(2013\)](#)). The effect of strain on thermal conductance would also be of interest in well-oriented polycrystalline thin films where the thermal conductivity is dominated by grain-boundary scattering.

References

- Abramson AR, Tien C, M. A. (2002). Interface and strain effects on the thermal conductivity of heterostructures: A molecular dynamics study. *ASME. J. Heat Transfer* 124(5), 963–970. (p. 37)
- Agrawal, R. and H. D. Espinosa (2011). Giant piezoelectric size effects in zinc oxide and gallium nitride nanowires. a first principles investigation. *Nano letters* 11(2), 786–790. (p. 42, 43)
- Alam, M., M. Manoharan, M. Haque, C. Muratore, and A. Voevodin (2012). Influence of strain on thermal conductivity of silicon nitride thin films. *Journal of Micromechanics and Microengineering* 22(4), 045001. (p. 6)
- Alam, M., R. Pulavarthy, C. Muratore, and M. Haque (2015). Mechanical strain dependence of thermal transport in amorphous silicon thin films. *Nanoscale and Microscale Thermophysical Engineering* 19(1), 1–16. (p. xiii, 6)
- Balandin, A. and K. L. Wang (1998). Effect of phonon confinement on the thermoelectric figure of merit of quantum wells. *Journal of Applied Physics* 84(11), 6149–6153. (p. 4)
- Bhowmick, S. and V. B. Shenoy (2006). Effect of strain on the thermal conductivity of solids. *The Journal of Chemical Physics* 125(16), –. (p. 37, 39, 40)
- Callaway, J. (1959). Model for lattice thermal conductivity at low temperatures. *Physical Review* 113(4), 1046. (p. 11)
- Carruthers, P. (1959). Scattering of phonons by elastic strain fields and the thermal resistance of dislocations. *Physical Review* 114(4), 995. (p. 12, 49)
- Cattaneo, C. (1958). Sur une forme de l’équation de la chaleur éliminant le paradoxe d’une propagation instantanée. *C. R. Acad. Sci.* 247, 431–433. (p. 27)
- Chalopin, Y., K. Esfarjani, A. Henry, S. Volz, and G. Chen (2012). Thermal interface conductance in si/ge superlattices by equilibrium molecular dynamics. *Physical Review B* 85(19), 195302. (p. 54)
- Chalopin, Y., N. Mingo, J. Diao, D. Srivastava, and S. Volz (2012). Large effects of pressure induced inelastic channels on interface thermal conductance. *Applied Physics Letters* 101(22), –. (p. 37)
- Chang, C., D. Okawa, A. Majumdar, and A. Zettl (2006). Solid-state thermal rectifier. *Science* 314(5802), 1121–1124. (p. 4)
- Che, J., T. Cagin, W. Deng, and W. A. Goddard (2000). Thermal conductivity of diamond and related materials from molecular dynamics simulations. *The Journal of Chemical Physics* 113(16), 6888–6900. (p. 27, 28)
- Cho, J., C. Richards, D. Bahr, J. Jiao, and R. Richards (2008). Evaluation of contacts for a mems thermal switch. *Journal of Micromechanics and Microengineering* 18(10), 105012. (p. xiii, 5)
- Dai, S., M. L. Dunn, and H. S. Park (2010). Piezoelectric constants for zno calculated using classical polarizable core-shell potentials. *Nanotechnology* 21(44), 445707. (p. 22)

- Dai, S., M. Gharbi, P. Sharma, and H. S. Park (2011). Surface piezoelectricity: size effects in nanostructures and the emergence of piezoelectricity in non-piezoelectric materials. *Journal of Applied Physics* 110(10), 104305. (p. 58)
- Dennard, R. H., V. Rideout, E. Bassous, and A. Leblanc (1974). Design of ion-implanted mosfet's with very small physical dimensions. *Solid-State Circuits, IEEE Journal of* 9(5), 256–268. (p. 1)
- Ding, H.-Q., N. Karasawa, and W. A. Goddard III (1992). Atomic level simulations on a million particles: The cell multipole method for coulomb and london non-bond interactions. *The Journal of chemical physics* 97(6), 4309–4315. (p. 21)
- Dresselhaus, M., G. Chen, M. Tang, R. Yang, H. Lee, D. Wang, Z. Ren, J.-P. Fleurial, and P. Gogna (2007). New directions for low-dimensional thermoelectric materials. *Advanced Materials* 19(8), 1043–1053. (p. 4)
- Ewald, P. P. (1921). Die berechnung optischer und elektrostatischer gitterpotentiale. *Annalen der Physik* 369(3), 253–287. (p. 21)
- Fennell, C. J. and J. D. Gezelter (2006). Is the ewald summation still necessary? pairwise alternatives to the accepted standard for long-range electrostatics. *The Journal of chemical physics* 124(23), 234104. (p. 21)
- Ftouni, H. (2015). *Transport thermique dans des membranes très minces de SiN amorphe*. Ph. D. thesis, NEEL - Institut Néel. (p. 6)
- Galan, U. and H. A. Sodano (2012). Molecular dynamics prediction of interfacial strength and validation through atomic force microscopy. *Applied Physics Letters* 101(15), 151603. (p. 58)
- Gale, J. D. and A. L. Rohl (2003). The general utility lattice program (gulp). *Molecular Simulation* 29(5), 291–341. (p. 22)
- Greiner, W. (2001). *Thermodynamics and Statistical Mechanics*. Springer. (p. 26)
- Gunes, M. and M. Ozenbas (2015). Effect of grain size and porosity on phonon scattering enhancement of ca 3 co 4 o 9. *Journal of Alloys and Compounds* 626, 360–367. (p. 4)
- Guo, J., C. Xu, B. Gu, and F. Sheng (2011). Structure evolution of zn cluster on graphene for zno nanostructure growth. *Journal of Applied Physics* 109(2), 024307. (p. 58)
- Harris, J. G. and K. H. Yung (1995). Carbon dioxide's liquid-vapor coexistence curve and critical properties as predicted by a simple molecular model. *The Journal of Physical Chemistry* 99(31), 12021–12024. (p. 58)
- Herzbach, D., K. Binder, and M. H. Muser (2005). Comparison of model potentials for molecular-dynamics simulations of silica. *The Journal of Chemical Physics* 123(12), –. (p. 22)
- Holland, M. (1963). Analysis of lattice thermal conductivity. *Physical Review* 132(6), 2461. (p. 11)
- Holzer, S. (2007). *Optimization for Enhanced Thermal Technology CAD Purposes*. Ph. D. thesis, Institut für Mikroelektronik. (p. xiii, 2)
- Hoover, W. G. (1985, Mar). Canonical dynamics: Equilibrium phase-space distributions. *Phys. Rev. A* 31, 1695–1697. (p. 18)
- Hsieh, W.-P., A. S. Lyons, E. Pop, P. Keblinski, and D. G. Cahill (2011). Pressure tuning of the thermal conductance of weak interfaces. *Physical Review B* 84(18), 184107. (p. 50)
- Ihlefeld, J. F., B. M. Foley, D. A. Scrymgeour, J. R. Michael, B. B. McKenzie, D. L. Medlin, M. Wallace, S. Troler-McKinstry, and P. E. Hopkins (2015). Room-

- temperature voltage tunable phonon thermal conductivity via reconfigurable interfaces in ferroelectric thin films. *Nano letters* 15(3), 1791–1795. (p. 4)
- Iskandar, A., A. Abou-Khalil, M. Kazan, W. Kassem, and S. Volz (2015). On the interplay between phonon-boundary scattering and phonon-point-defect scattering in sige thin films. *Journal of Applied Physics* 117(12), 125102. (p. 4)
- J., B. D. (1994). *Computational modelling of zinc oxide and related oxide ceramics*. Ph. D. thesis, University of Surrey. (p. 21, 22)
- Jedrecy, N., M. Sauvage-Simkin, and R. Pinchaux (2000). The hexagonal polar zno (0001)-(1 × 1) surfaces: structural features as stemming from x-ray diffraction. *Applied surface science* 162, 69–73. (p. 58)
- Jiang, J.-W., H. S. Park, and T. Rabczuk (2013). Polar surface effects on the thermal conductivity of zno nanowires: a shell-like surface reconstruction-induced preserving mechanism. *Nanoscale* 5(22), 11035–11043. (p. 59)
- Kapitza, P. (1941). Heat transfer and superfluidity of helium ii. *Physical Review* 60(4), 354. (p. 47)
- Kazan, M. (2011). Interpolation between the acoustic mismatch model and the diffuse mismatch model for the interface thermal conductance: Application to inn/gan superlattice. *Journal of Heat Transfer* 133(11), 112401. (p. 48)
- Keyes, R. W. and R. J. Sladek (1962, Jan). Piezo-thermal conductivity effect in germanium. *Phys. Rev.* 125, 478–483. (p. 6)
- Kim, W., J. Zide, A. Gossard, D. Klenov, S. Stemmer, A. Shakouri, and A. Majumdar (2006). Thermal conductivity reduction and thermoelectric figure of merit increase by embedding nanoparticles in crystalline semiconductors. *Physical Review Letters* 96(4), 045901. (p. 4)
- Klemens, P. (1951). The thermal conductivity of dielectric solids at low temperatures (theoretical). In *Proceedings of the Royal Society of London A: Mathematical, Physical and Engineering Sciences*, Volume 208, pp. 108–133. The Royal Society. (p. 11)
- Kobayashi, W., Y. Teraoka, and I. Terasaki (2010). A trial thermal rectifier. *Journal of electronic materials* 39(9), 1488–1492. (p. 4)
- Kobiakov, I. (1980). Elastic, piezoelectric and dielectric properties of zno and cds single crystals in a wide range of temperatures. *Solid State Communications* 35(3), 305 – 310. (p. 24)
- Kubo, R., M. Toda, and N. Hashitsume (1985). *Statistical Physics II*. Springer, Berlin. (p. 26, 27)
- Kulkarni, A. J. and M. Zhou (2006). Surface-effects-dominated thermal and mechanical responses of zinc oxide nanobelts. *Acta Mechanica Sinica* 22(3), 217–224. (p. 22, 58)
- Kulkarni, A. J. and M. Zhou (2007). Tunable thermal response of zno nanowires. *Nanotechnology* 18(43), 435706. (p. 5)
- Landry, E. and A. McGaughey (2010). Effect of film thickness on the thermal resistance of confined semiconductor thin films. *Journal of Applied Physics* 107(1), 013521. (p. 54)
- Lauritsen, J. V., S. Porsgaard, M. K. Rasmussen, M. C. Jensen, R. Bechstein, K. Meinander, B. S. Clausen, S. Helveg, R. Wahl, G. Kresse, et al. (2011). Stabilization principles for polar surfaces of zno. *ACS nano* 5(7), 5987–5994. (p. 58)

- Li, J., L. Porter, and S. Yip (1998). Atomistic modeling of finite-temperature properties of crystalline b-sic ii. thermal conductivity and effects of point defects. *The Journal of Chemical Physics* 255, 139–152. (p. 27)
- Li, N., J. Ren, L. Wang, G. Zhang, P. Hänggi, and B. Li (2012, Jul). Colloquium : Phononics: Manipulating heat flow with electronic analogs and beyond. *Rev. Mod. Phys.* 84, 1045–1066. (p. 4)
- Li, S., X. Ding, J. Ren, X. Moya, J. Li, J. Sun, and E. K. Salje (2014). Strain-controlled thermal conductivity in ferroic twinned films. *Scientific reports* 4. (p. 4)
- Li, X., K. Maute, M. L. Dunn, and R. Yang (2010a, Jun). Strain effects on the thermal conductivity of nanostructures. *Phys. Rev. B* 81, 245318. (p. 5)
- Li, X., K. Maute, M. L. Dunn, and R. Yang (2010b, Jun). Strain effects on the thermal conductivity of nanostructures. *Phys. Rev. B* 81, 245318. (p. 37)
- Lynch, W. (1972). Calculation of electric field breakdown in quartz as determined by dielectric dispersion analysis. *Journal of Applied Physics* 43(8), 3274–3278. (p. 64)
- Mak, K. F., C. H. Lui, and T. F. Heinz (2010). Thermal conductance at the graphene-sio2 interface measured by optical pump-probe spectroscopy. *arXiv preprint arXiv:1009.0231*. (p. 51, 54, 57, 60)
- Maldovan, M. (2013). Sound and heat revolutions in phononics. *Nature* 503(7475), 209–217. (p. xiii, 3)
- McGaughey, A. and M. Kaviani (2004). Thermal conductivity decomposition and analysis using molecular dynamics simulations. part i. lennard-jones argon. *International Journal of Heat and Mass Transfer* 47(8-9), 1783 – 1798. (p. xiii, 27, 28)
- McMenamin, A. (2013, April). The end of dennard scaling. web. (p. 1)
- Meng, Q., L. Wu, and Y. Zhu (2013). Phonon scattering of interfacial strain field between dissimilar lattices. *Physical Review B* 87(6), 064102. (p. xiv, 49, 50, 65)
- Müller-Plathe, F. (1997). A simple nonequilibrium molecular dynamics method for calculating the thermal conductivity. *The Journal of Chemical Physics* 106(14), 6082–6085. (p. 33)
- Momeni, K., G. M. Odegard, and R. S. Yassar (2012). Finite size effect on the piezoelectric properties of zno nanobelts: A molecular dynamics approach. *Acta Materialia* 60(13–14), 5117 – 5124. (p. 22)
- Moore, G. E. (2006, Sept). Cramming more components onto integrated circuits, reprinted from electronics, volume 38, number 8, april 19, 1965, pp.114 ff. *Solid-State Circuits Society Newsletter, IEEE* 11(5), 33–35. (p. 1)
- Morkoc, H. and U. Ozgur (2009). *Zinc Oxide Fundamentals, Materials and Device Technology*. Wiley-VCH. (p. 36)
- Müllen, K. and U. Scherf (2006). *Organic light emitting devices: synthesis, properties and applications*. John Wiley & Sons. (p. 2)
- Newnham, R. E. (2005). *Properties of Materials: Anisotropy, Symmetry, Structure* (1 ed.). Oxford University Press. (p. xiii, 13, 14)
- Noguera, C. (2000). Polar oxide surfaces. *Journal of Physics: Condensed Matter* 12(31), R367. (p. 58)
- Ong, Z.-Y. and E. Pop (2010, Apr). Molecular dynamics simulation of thermal boundary conductance between carbon nanotubes and sio₂. *Phys. Rev. B* 81, 155408. (p. 55)

- Ozgur, ., X. Gu, S. Chevtchenko, J. Spradlin, S.-J. Cho, H. Morkoc, F. Pollak, H. Everitt, B. Nemeth, and J. Nause (2006). Thermal conductivity of bulk zno after different thermal treatments. *Journal of Electronic Materials* 35(4), 550–555. (p. 35, 36)
- Parrish, K. D., A. Jain, J. M. Larkin, W. A. Saidi, and A. J. H. McGaughey (2014, Dec). Origins of thermal conductivity changes in strained crystals. *Phys. Rev. B* 90, 235201. (p. 5, 37, 39, 41, 64)
- Pernot, G., M. Stoffel, I. Savic, F. Pezzoli, P. Chen, G. Savelli, A. Jacquot, J. Schumann, U. Denker, I. Mönch, C. Deneke, O. G. Schmidt, J. M. Rampnoux, S. Wang, M. Plissonnier, A. Rastelli, S. Dilhaire, and N. Mingo (2010, Jun). Precise control of thermal conductivity at the nanoscale through individual phonon-scattering barriers. *Nat Mater* 9(6), 491–495. (p. 4)
- Plimpton, S. (1995). Fast parallel algorithms for short-range molecular dynamics. *Journal of Computational Physics* 117(1), 1 – 19. (p. 26)
- Rajabpour, A. and S. Volz (2010). Thermal boundary resistance from mode energy relaxation times: Case study of argon-like crystals by molecular dynamics. *Journal of Applied Physics* 108(9), 094324. (p. 56, 57)
- Rosen, M. and H. Klimker (1970, May). Low-temperature elasticity and magnetoelasticity of dysprosium single crystals. *Phys. Rev. B* 1, 3748–3756. (p. 41)
- Sääskilähti, K., J. Oksanen, J. Tulkki, and S. Volz (2014). Role of anharmonic phonon scattering in the spectrally decomposed thermal conductance at planar interfaces. *Physical Review B* 90(13), 134312. (p. 50)
- Sarasamak, K., S. Limpijumnong, and W. R. L. Lambrecht (2010, Jul). Pressure-dependent elastic constants and sound velocities of wurtzite sic, gan, inn, zno, and cdse, and their relation to the high-pressure phase transition: A first-principles study. *Phys. Rev. B* 82, 035201. (p. 38)
- Schelling, P. K., S. R. Phillpot, and P. Keblinski (2002, Apr). Comparison of atomic-level simulation methods for computing thermal conductivity. *Phys. Rev. B* 65, 144306. (p. 29)
- Schelling, P. K., L. Shi, and K. E. Goodson (2005). Managing heat for electronics. *Materials Today* 8(6), 30 – 35. (p. xiii, 3)
- Serrano, e. a. (2004). Pressure dependence of the lattice dynamics of zno: An ab initio approach. *Physical Review B* 69(9), 094306. (p. 22, 23, 36)
- Shen, M., W. J. Evans, D. Cahill, and P. Keblinski (2011, Nov). Bonding and pressure-tunable interfacial thermal conductance. *Phys. Rev. B* 84, 195432. (p. 37, 50, 60)
- Shen, M., P. K. Schelling, and P. Keblinski (2013). Heat transfer mechanism across few-layer graphene by molecular dynamics. *Physical Review B* 88(4), 045444. (p. 51, 54, 60)
- Slack, G. A. (1972, Nov). Thermal conductivity of ii-vi compounds and phonon scattering by Fe^{2+} impurities. *Phys. Rev. B* 6, 3791–3800. (p. 35)
- Slack, G. A., L. J. Schowalter, D. Morelli, and J. A. F. Jr. (2002). Some effects of oxygen impurities on aln and gan. *Journal of Crystal Growth* 246(3–4), 287 – 298. Proceedings of the International Workshop on Bulk Nitride Semiconductors. (p. 44)
- Slack, G. A., R. Tanzilli, R. Pohl, and J. Vandersande (1987). The intrinsic thermal conductivity of {AlN}. *Journal of Physics and Chemistry of Solids* 48(7), 641 – 647. (p. 44)

- Slater, J. C. and J. G. Kirkwood (1931, Mar). The van der waals forces in gases. *Phys. Rev.* *37*, 682–697. (p. 21)
- Smalley, R. E. (2005, 6). Future global energy prosperity: The terawatt challenge. *MRS Bulletin* *30*, 412–417. (p. 3)
- Srivastava, G. P. (1990). *The physics of phonons*. CRC Press. (p. xiii, 7, 10, 11, 12, 48)
- Stackhouse, S. and L. Stixrude (2010). Theoretical methods for calculating the lattice thermal conductivity of minerals. *Reviews in Mineralogy and Geochemistry* *71*(1), 253–269. (p. 34)
- Stuart, S. J., A. B. Tutein, and J. A. Harrison (2000). A reactive potential for hydrocarbons with intermolecular interactions. *The Journal of chemical physics* *112*(14), 6472–6486. (p. 55)
- Suriano, F., M. Ferri, F. Moscatelli, F. Mancarella, L. Belsito, S. Solmi, A. Roncaglia, S. Frabboni, G. Gazzadi, and D. Narducci (2015). Influence of grain size on the thermoelectric properties of polycrystalline silicon nanowires. *Journal of Electronic Materials* *44*(1), 371–376. (p. 4)
- Taylor, G. (2009). Energy efficient circuit design and the future of power delivery. EPEPS 2009. Intel. (p. 1)
- Termentzidis, K. and S. Merabia (2012). *Molecular Dynamics Simulations and Thermal Transport at the Nano-Scale*. InTech. (p. 29, 45)
- Tersoff, J. (1989, Mar). Modeling solid-state chemistry: Interatomic potentials for multicomponent systems. *Phys. Rev. B* *39*, 5566–5568. (p. 51)
- Tu, Z. C. and X. Hu (2006, Jul). Elasticity and piezoelectricity of zinc oxide crystals, single layers, and possible single-walled nanotubes. *Phys. Rev. B* *74*, 035434. (p. 24)
- Tungare, M., Y. Shi, N. Tripathi, P. Suvarna, and F. S. Shahedipour-Sandvik (2011). A tersoff-based interatomic potential for wurtzite aln. *physica status solidi (a)* *208*(7), 1569–1572. (p. 24)
- van Beest, B. W. H., G. J. Kramer, and R. A. van Santen (1990, Apr). Force fields for silicas and aluminophosphates based on *ab initio* calculations. *Phys. Rev. Lett.* *64*, 1955–1958. (p. 21, 22, 55)
- Van Zwol, P., K. Joulain, P. B. Abdallah, J. Greffet, and J. Chevrier (2011). Fast nanoscale heat-flux modulation with phase-change materials. *Physical Review B* *83*(20), 201404. (p. 4)
- Vashishta, P., R. K. Kalia, A. Nakano, and J. P. Rino (2007). Interaction potential for silicon carbide: A molecular dynamics study of elastic constants and vibrational density of states for crystalline and amorphous silicon carbide. *Journal of Applied Physics* *101*(10), –. (p. 22)
- Vashishta, P., R. K. Kalia, A. Nakano, and J. P. Rino (2011). Interaction potential for aluminum nitride: A molecular dynamics study of mechanical and thermal properties of crystalline and amorphous aluminum nitride. *Journal of Applied Physics* *109*(3), –. (p. xiii, 22, 24, 25, 26, 43, 45)
- Vashishta, P., R. K. Kalia, J. P. Rino, and I. Ebbsjö (1990, Jun). Interaction potential for SiO_2 : A molecular-dynamics study of structural correlations. *Phys. Rev. B* *41*, 12197–12209. (p. 22)
- Venkatasubramanian, R. (2000). Lattice thermal conductivity reduction and phonon localizationlike behavior in superlattice structures. *Physical Review B* *61*(4), 3091. (p. 4)

- Vernotte, P. (1958). Les paradoxes de la theorie continue de l'equation de la chaleur. *C. R. Acad. Sci.* 246, 3154–3155. (p. 27)
- Volz, S. (2009). *Thermal nanosystems and nanomaterials*, Volume 118. Springer Science & Business Media. (p. 26)
- Volz, S., J.-B. Saulnier, M. Lallemand, B. Perrin, P. Depondt, and M. Mareschal (1996, Jul). Transient fourier-law deviation by molecular dynamics in solid argon. *Phys. Rev. B* 54, 340–347. (p. 27)
- Wang, L. and B. Li (2007). Thermal logic gates: computation with phonons. *Physical review letters* 99(17), 177208. (p. 4)
- Wang, S., Z. Fan, R. S. Koster, C. Fang, M. A. Van Huis, A. O. Yalcin, F. D. Tichelaar, H. W. Zandbergen, and T. J. Vlugt (2014). New ab initio based pair potential for accurate simulation of phase transitions in zno. *The Journal of Physical Chemistry C* 118(20), 11050–11061. (p. xi, 23, 24, 36)
- Weng, C.-J. (2009). Advanced thermal enhancement and management of {LED} packages. *International Communications in Heat and Mass Transfer* 36(3), 245 – 248. (p. 2)
- Wolf, D., P. Keblinski, S. Phillpot, and J. Eggebrecht (1999). Exact method for the simulation of coulombic systems by spherically truncated, pairwise r-1 summation. *The Journal of chemical physics* 110(17), 8254–8282. (p. 21)
- Wolf, M. W. and J. J. Martin (1973). Low temperature thermal conductivity of zinc oxide. *physica status solidi (a)* 17(1), 215–220. (p. 35, 36)
- Wu, H., J. Carrete, Z. Zhang, Y. Qu, X. Shen, Z. Wang, L.-D. Zhao, and J. He (2014). Strong enhancement of phonon scattering through nanoscale grains in lead sulfide thermoelectrics. *NPG Asia Materials* 6(6), e108. (p. 4)
- Xu, Y. and G. Li (2009). Strain effect analysis on phonon thermal conductivity of two-dimensional nanocomposites. *Journal of Applied Physics* 106(11), –. (p. 37)
- Yuan, L., S. Liu, M. Chen, and X. Luo (2006, Aug). Thermal analysis of high power led array packaging with microchannel cooler. In *Electronic Packaging Technology, 2006. ICEPT '06. 7th International Conference on*, pp. 1–5. (p. 2)

